UNIVERSITÀ
DEGLI STUDI
FIRENZE

Scuola di Scienze Matematiche
Fisiche e Naturali

Master Degree in Physical
and Astrophysical Sciences

First experimental steps for a neutral atoms based quantum computer

Candidate:
Alessandro Vanni

Supervisor:
Leonardo Fallani

Co-supervisor:
Luca Tanzi

Academic year: 2024/2025

Contents

Introduction **1**

1 Theoretical background **5**
1.1 Laser cooling 5
1.1.1 Zeeman slower 7
1.1.2 Magneto-optical trap 7
1.2 Optical tweezers 9
1.2.1 Optical tweezer production 10
1.2.2 Optical tweezer loading and rearrangement 11
1.3 Feedback control systems 12
1.3.1 PID 13
1.4 Pound–Drever–Hall technique 15
1.4.1 Principle 16
1.4.2 Quantitative model 16
1.4.3 Modulation frequency and regimes 17
1.4.4 Implementation 18

2 Experimental setup project **21**
2.1 Ytterbium 21
2.2 Atom cooling stages 22
2.3 Rydberg atoms 24
2.4 Quantum gates 26
2.4.1 Single-qubit gates 26
2.4.2 multi-qubit gates 30
2.5 The platform 32

3 Vacuum system **37**
3.1 General description of the system 37
3.1.1 Atomic source 39
3.1.2 Pumping chamber 40
3.1.3 Glass cell 41
3.2 Assembly of a ultra-high vacuum system 42
3.3 Pumping and bakeout 43

4 Laser system **47**
4.1 Blue laser 48
4.1.1 Spectroscopy 50
4.1.2 Frequency lock 51
4.1.3 2D MOT 53
4.1.4 Zeeman slower 54
4.2 Green laser 56
4.2.1 ULE cavity 57
4.2.2 Lock on ULE cavity 61
4.2.3 Offset lock 64

5 First observation of the atoms **67**
5.1 Atomic beam slowing and alignment 67
5.2 First attempts to detect atoms in the glass cell 69
5.3 399 nm 3D MOT 72

Conclusions and future perspectives **75**

Introduction

Quantum computing [1] has seen rapid advancements in recent years, as it offers a promising approach to solving problems that are intractable for classical computation due to either their inherent quantum nature or their computational complexity. There are several platforms on which research toward the realization of a quantum computer is being conducted in parallel. One of the most promising at present is the atom-based platform. In these systems, the qubit state is encoded in the internal state of individual atoms, the two logical states $|0\rangle$ and $|1\rangle$ corresponding to two long-lived atomic states, chosen in such a way to ensure long coherence times.

To perform logical operations using atoms as qubits, it is necessary to trap individual atoms and be able to induce both global and selective excitations and readout. Two key ingredients are used to achieve this: optical tweezers and Rydberg excitations. Optical tweezers are highly focused laser beams capable of trapping single atoms and rearranging them into arbitrarily shaped arrays. An example of an array of atoms trapped in optical tweezers and a process of tweezers rearrangement are shown in Fig. 0.1 and Fig. 0.2.

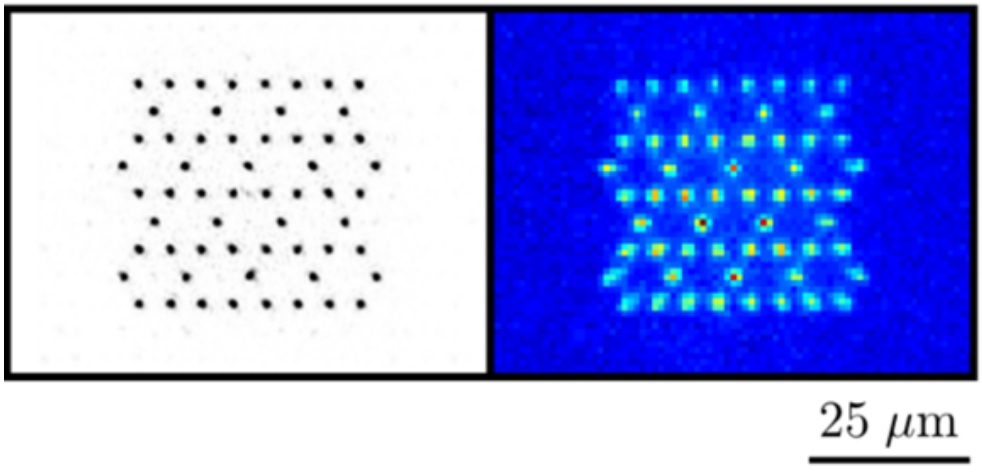

Figure 0.1. Single atoms trapped in an arbitrary shaped optical tweezers 2D array. Figure from ref. [2].

These systems offer remarkable scalability with state-of-the-art experiments successfully trapping thousands of individual atoms [4], a crucial feature in the pursuit of a high qubit number, which is essential for building a universal

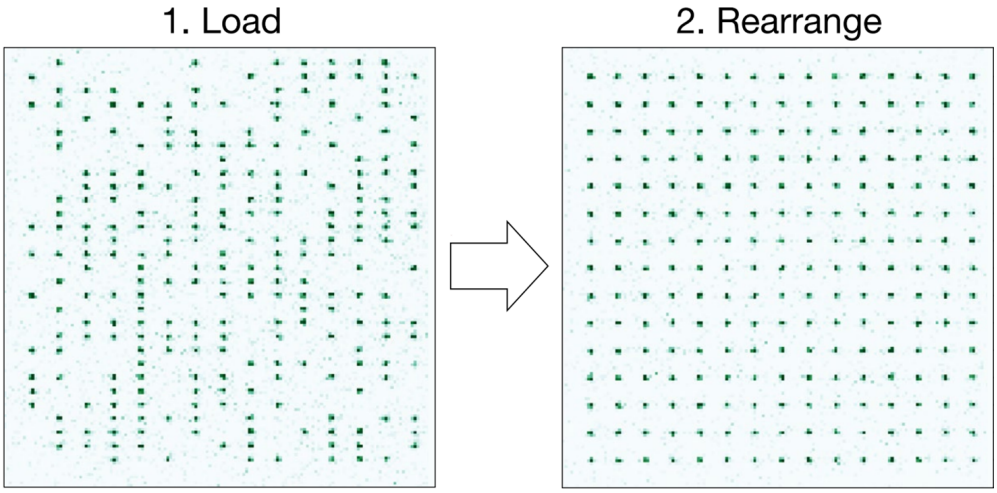

Figure 0.2. Process of rearrangement. Exploiting particular devices it is possible to arbitrarily reshape optical tweezer arrays without losing atoms form the traps. Figure from ref. [3].

fault-tolerant quantum computer. The ability to address single atoms is fundamental for quantum computing, as it is necessary to implement both single- and multi-qubit gates, which require selectively exciting individual atoms or atom pairs.

The other essential component for entangling qubits are Rydberg excitations, which are excitations to states with high principal quantum number $n \gg 1$, slightly below the ionization continuum. In these states the mean radius of the electron wavefunction increases as n^2, leading to a fast increase of the short-range atom-atom Var der Waals interaction as n^{11}. As a result, two Rydberg atoms with $n>50$ localized in two nearby optical tweezers (typically they need to be separated by a few micrometers to be optically resolved), can experience a substantial interaction energy exceeding the MHz scale. This energy shift, larger than the transition linewidth, leads to the so-called "Rybderg blockade" effect, e.g. the impossibility for a resonant laser to excite an atom to the Rydberg state when another nearby atom has already been excited, eventually leading to quantum entanglement between the atoms.

My thesis was carried out in a newly established laboratory at the Department of Physics and astronomy of the university of Florence, where I took part in the initial stages of an atomic physics experiment aimed at developing a platform for quantum computation based on neutral ^{171}Yb atoms. These stages correspond to the design and construction of the vacuum apparatus, which consists of a commercial ytterbium atomic source connected to a pumping chamber and a science cell, and of the laser system, needed for the initial cooling stages of the atoms. The thesis is organized as follows: Chapter 1 lays the theoretical foundations necessary to understand both the experiment as a whole and the first steps effectively undertaken during this work. Chapter 2

introduces the experimental project in order to clarify all the stages described in the subsequent chapters of the thesis. Chapter 3 describes the configuration of the experimental apparatus, with particular focus on the procedures employed in constructing the vacuum system. Chapter 4 details the laser setup, specifically the components realized so far and their applications in the initial stages of laser cooling. It also explains all the techniques employed for laser frequency stabilization. Finally, Chapter 5 shows the first observation of atoms in the experiment, with detailed explanation of all the critical points that have to be addressed in order to to ensure the proper operation of the system.

Chapter 1

Theoretical background

This chapter will focus on the introduction of the main theoretical aspects one has to know to understand the experimental phases of the thesis. In particular, the focus will be on atom-cooling techniques, going in the details of those used in the experiment, and on control systems and laser stabilization techniques based on Pound-Drever-Hall scheme.

1.1 Laser cooling

Laser cooling techniques rely mainly on radiative forces, which make it possible to dissipate the kinetic energy of the atoms and to confine them. Radiative forces are divided in two main contributes: radiation pressure force (dissipative) and optical dipole force (conservative)[5]:

$$F_{rp} = -\frac{\hbar\Omega\nabla\phi}{2}\frac{\Omega\frac{\gamma}{2}}{\delta^2+\frac{\gamma^2}{4}+\frac{\Omega^2}{2}} \tag{1.1}$$

$$F_{od} = -\frac{\hbar\nabla\Omega}{2}\frac{\Omega\delta}{\delta^2+\frac{\gamma^2}{4}+\frac{\Omega^2}{2}} \tag{1.2}$$

Let's clarify what each of these variables represent:

- Ω is the Rabi frequency of the interaction and it is given by: $\frac{e\vec{E}_0\cdot\vec{\mu}_{eg}}{\hbar}$, where $\vec{\mu}_{eg}$ is the transition matrix element between the two states of the two-level system and $\vec{E}_0$ is the amplitude of the laser light electric field;
- ϕ is the phase of the electric field interacting with the atoms;
- γ is the spontaneous emission rate;
- δ is the detuning of the light from the transition frequency: $\delta = \omega - \omega_0$ where ω is the light (angular) frequency and ω_0 is the (angular) frequency of the atomic transition.

Radiation pressure force can also be written as a function of the saturation ratio $s = \frac{I}{I_{sat}}$ where $I_{sat} = \frac{\pi hc}{3\lambda^3 \tau}$ as:

$$F_{rp} = \hbar \vec{k} \frac{\gamma}{2} \frac{s}{1+s} \frac{1}{1+\left(\frac{2\delta}{\gamma_s}\right)^2} \tag{1.3}$$

with γ_s saturated linewidth of the transition and $\vec{k}$ wave vector of the radiation. Looking at this equation it is clear that the radiation pressure force has a saturation point when the intensity of the laser reaches I_{sat}. Being a dissipative force, it is mainly used to slow down the atoms, as it happens in optical molasses, where the atoms are trapped at temperatures that can reach a minimum of around microkelvin (depending on the chosen atomic species); this is because the temperature is limited by fluctuations in photon scattering, whose frequency depends on the linewidth of the transition used and on the detuning. The minimum temperature reachable with these techniques is the Doppler temperature:

$$T_D = \frac{\hbar \gamma}{2K_B} \tag{1.4}$$

unless sub-Doppler techniques are implemented.

The otical dipole force is a conservative force and it is used to trap atoms with far detuned light. Since it is conservative it can be written as the gradient of a scalar function:

$$U_{od} = \frac{\hbar \delta}{2} \ln\left(1 + \frac{\frac{\Omega^2}{2}}{\delta^2 + \frac{\gamma^2}{4}}\right) \tag{1.5}$$

when the detuning is large ($\delta \gg \Omega, \gamma$) the optical dipole potential becomes:

$$U_{od} = \frac{\hbar \Omega^2}{4\delta} \propto I\left(\vec{R}\right) \tag{1.6}$$

This means that the atoms will feel a maximum of the trapping potential where the intensity of the laser is maximum (or minimum, depending on the sign of the detuning).

It should be noted that, since the laser interacting with the atoms is typically far off-resonance, the two–level system approximation is no longer valid, and it is therefore necessary to take into account the contributions of all relevant atomic states:

$$U_{od} = \sum_{i \neq g} \frac{\hbar \Omega_i^2}{4\delta_i} \tag{1.7}$$

1.1.1 Zeeman slower

In most of the experimental configurations (including that studied in this thesis) the atomic source is represented by an atomic beam, i.e. a collimated stream of atoms, which, for sake of simplicity, we will consider moving all with the same velocity $\vec{v_0}$ along the x direction. To slow the atoms, a counterpropagating resonant laser beam can be used. Since the atoms are moving, it is necessary to account for the Doppler shift in the atomic transition. However, as the atoms are slowed down by the radiation pressure force, the Doppler shift changes. To keep the atoms resonant with the laser an inhomogeneous magnetic field $\vec{B}$ is introduced. Considering the anomalous Zeeman effect for weak $\vec{B}$ fields the shift is:

$$\Delta\mu B = (g_{fe}m_{fe} - g_{fg}m_{fg})\mu_B B \tag{1.8}$$

where μ_B is the Bohr magneton, g_f is the Landé g-factor, m_f is the z component of the hyperfine total angular momentum and the subscripts g and f indicate ground and excited state of the two-level system. The resonance condition in the atoms' frame is:

$$\omega + kv = \omega_0 + \tfrac{\Delta\mu}{\hbar}B \tag{1.9}$$

$$\delta = \omega - \omega_0 = \tfrac{\Delta\mu}{\hbar}B - kv = -kv_0 \tag{1.10}$$

The force exerted on the atoms for $s \gg 1$ is $\vec{F} = \hbar\vec{k}\frac{\gamma}{2}$, and, solving the equation of motion, we obtain:

$$v(x) = \sqrt{v_0^2 - 2ax} \tag{1.11}$$

where a is the acceleration of the atoms. Therefore, the atoms stop after $L = \frac{v_0^2}{2a}$. It follows:

$$B\left(x\right) = B_0\left(\sqrt{1 - \tfrac{x}{L}} - 1\right) \tag{1.12}$$

with $B_0 = \frac{\hbar k v_0}{\Delta\mu}$.

This process will constitute the first cooling stage of this experiment and its realization will be presented in the following chapters.

1.1.2 Magneto-optical trap

Magneto-optical traps are dissipative traps that exploit the radiation pressure force combined with a magnetic field to cool and confine the atoms. The schematic idea is presented in Fig. 1.1.

Considering a two-level system whose excited state has total angular momentum $J = 1$ (as in the bosonic isotopes of Yb), its Zeeman splitting consists of three sublevels, one for each value of the angular momentum projection quantum number m_J. Introducing a magnetic field $\vec{B} = b\vec{x}$ the splitting of the levels is gonna look like the structure represented in Fig. 1.1. Now consider two counterpropagating beams along the x direction, whose polarization is circular

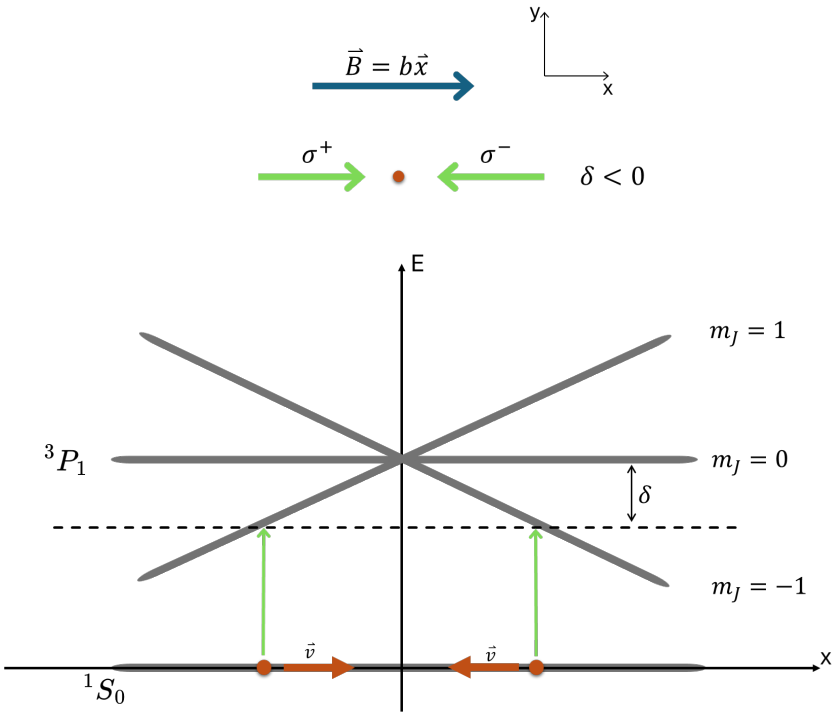

Figure 1.1. Schematic representation of a magneto-optical trap working principle for a bosonic isotope of Yb.

righthanded for that with $\vec{k} = k\hat{x}$ and circular lefthanded for the other. If the beams are red-detuned ($\delta < 0$), the atoms in $x > 0$ are nearly resonant with the σ^- polarization beam, while atoms in $x < 0$ are nearly resonant with the σ^+ polarization beam; meaning all the atoms feel a radiation pressure force toward $x = 0$. Mathematically, by simply summing up the contribute of the two beams to the radiation pressure force, one obtains:

$$\vec{F} = \vec{F_1} + \vec{F_2} = \hbar\vec{k}\frac{\gamma}{2}\left(\frac{s}{1+\frac{4\left(\omega-\left(\omega_0+kv+g_{f_e}\mu_B bx\right)\right)^2}{\gamma^2}} - \frac{s}{1+\frac{4\left(\omega-\left(\omega_0-kv-g_{f_e}\mu_B bx\right)\right)^2}{\gamma^2}}\right) \approx (M\Omega^2 x - \alpha v)\hat{x}$$

which is a damped harmonic oscillator force with friction coefficient:

$$\alpha = -8\hbar k^2 s \frac{\frac{\delta}{\gamma}}{1+\frac{4\delta^2}{\gamma^2}} \tag{1.13}$$

damping time:

$$\tau = \frac{M}{\alpha} \tag{1.14}$$

where M is the mass, and trap frequency:

$$\Omega = \sqrt{\frac{g_{f_e}\mu_B b}{\hbar k M}\alpha} \tag{1.15}$$

In this thesis experiment, a 2D MOT and a 3D MOT will be implemented: the latter with the purpose of collimating the atomic beam and deflect it towards the final position of the experiment, and the latter to trap and cool atoms down to the Doppler temperature of the transition chose. More details on the MOTs setup of this thesis are given in chapter 2 and 4.

1.2 Optical tweezers

Optical tweezers [6] are optical dipole traps. They are created by highly focused laser beams, whose trapping potential is given by the optical dipole potential:

$$U = \sum_{i \neq g} \frac{\hbar \Omega_i^2}{4\delta_i} \tag{1.16}$$

Here the subscript i refers to any electronic state for which there is a non-negligible dipole matrix element to the state g, for which one is calculating the trapping potential. In the case where the trap wavelength is red-detuned from a given atomic transition ($\delta_i < 0$) the contribution to the trapping potential from that transition will be attractive (i.e. the atom will be attracted to regions of higher laser intensity). If the trap wavelength of the optical tweezer is chosen such that the net trapping potential is attractive, then atoms will be trapped by the Gaussian intensity profile of a tightly focused laser beam. The trapping potential is often rewritten in terms of the state polarizability, α, and the beam intensity, I:

$$U = -\tfrac{1}{4} h \alpha I(r, z) \tag{1.17}$$

For a Gaussian beam the spatial intensity profile is given by:

$$I(r, z) = \frac{2P_0}{\pi w(z)^2} e^{-\frac{2r^2}{w(z)^2}} \tag{1.18}$$

Here P_0 is the laser power, and $w(z)$ represents $\frac{1}{e^2}$ beam radius, which is related to the beam-waist at the focus (w_0) by:

$$w(z) = \sqrt{1 + \left(\frac{\lambda z}{\pi \omega_0^2}\right)^2} \tag{1.19}$$

We define the trap depth, U_0, as the magnitude of the trap potential at the focus:

$$U_0 = |U(r = 0, z = 0)| = \frac{h P_0 \alpha}{2\pi \omega_0^2} \tag{1.20}$$

A crucial condition for an atom being trapped in optical tweezers is that the temperature of the atom is much below the trap depth ($k_b T \ll h U_0$).

1.2.1 Optical tweezer production

One of the attractive capabilities of optical tweezers is the ability to arrange and reconfigure individual tweezers in different array geometries via the use of acousto-optic deflectors (AOD) and spatial light modulators (SLM). In the case of AODs multi-tone radio frequencies generate multiple diffracted beams, which each enter a high-NA microscope objective at a different angle, leading to a different position for each diffracted beam in the focal plane. Thus, through the use of an arbitrary waveform generator (AWG), one can design RF waveforms that allow for an arbitrary arrangement of many optical tweezers in 1D. Furthermore, due to the ability to rapidly change the AWG waveform driving the AOD, the geometry of the 1D tweezer array can also be reconfigured during a given experimental sequence [7], as shown in Fig. 1.2. Dynamic reconfigurability of tweezer geometries is a necessary condition for generating large-scale defect free arrays of trapped atoms.

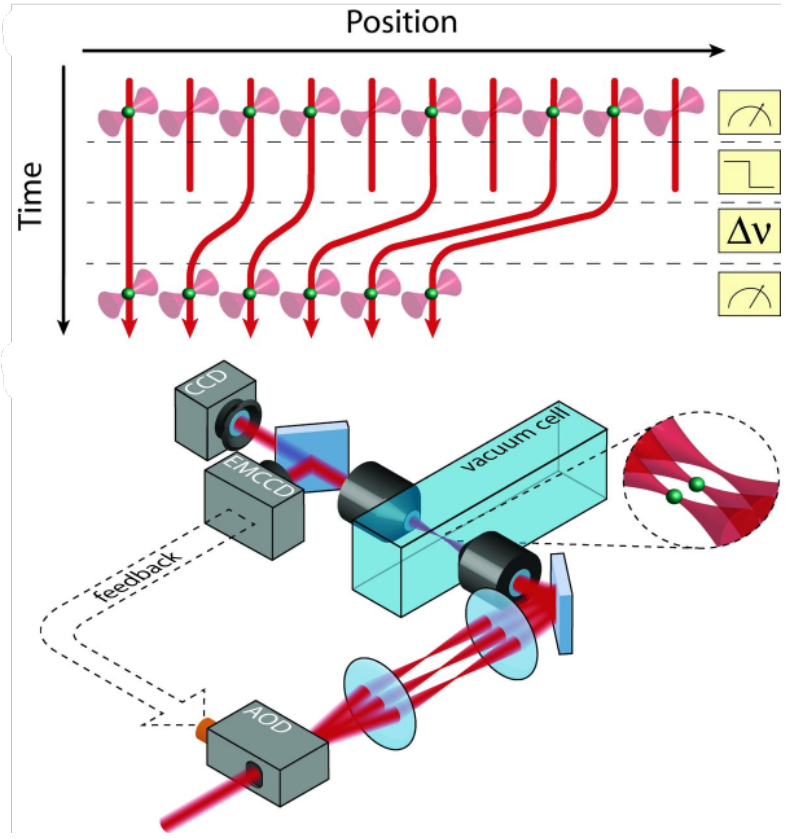

Figure 1.2. Shcematics of a setup for optical tweezers generation and rearrangement with an acusto-optic deflector. Fig. from Ref. [7].

1.2.2 Optical tweezer loading and rearrangement

Loading of optical tweezers from a cold atomic gas is a fundamentally stochastic process. Atoms are initially loaded from the atomic gas trapped in a MOT, however, it is possible that more than one atom is trapped inside a tweezer. To solve this problem, a process known as light-assisted collision will be used. It consists in ejecting pairs of atoms by exciting them to a molecular bound state, leading to a parity projection, which leaves either 0 or 1 atom in each tweezer trap [8, 9]; a schematics of the process is shown in Fig. **??**.

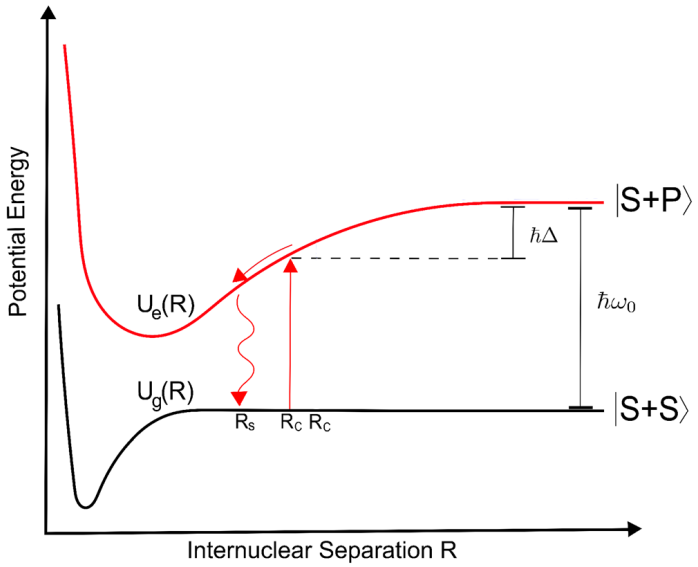

Figure 1.3. Schematic representation of light-assisted collisions mechanism. During the collision of two atoms, the laser excites one of the two to an excited state we call P. The atoms form a loosely bound pair with one atom in the S state (ground state) and the other in the P state and interact through the long-range dipole-dipole attractive potential $V(R) = -\frac{C_3}{R^3}$ (here, R is the interatomic distance, $C_3 = \frac{3\hbar\Gamma}{4k^3}$, $\frac{\Gamma}{2\pi}$ is the linewidth of the P state, and λ is the wavelength of the $S \rightarrow P$ transition). If the kinetic energy acquired by an atom pair before it radiates back to the ground state exceeds the optical dipole trap depth U, it escapes the trap, thus leading to the loss of two atoms.

Once single atoms are trapped into stochastically loaded optical tweezers, rearrangement is needed in order to create defect-free arrays of atoms. A common technique to engineering defect-free 1D arrays is to take a fluorescence image of a loaded tweezer array, then turn off RF tones associated with empty sites, followed by ramping the RF tones of filled sites such that they occupy the desired positions in the final array. Using a pair of orthogonal AODs allows for the creation of rectangular 2D arrays, however, the ability to reconfigure into defect-free arrays is complicated by the fact that turning off a single RF tone will turn off an entire row or column of tweezers, not just a single site. A solution to this problem is to combine the capabilities of a SLM and a pair of orthogonal AODs. By varying the phase pattern on a SLM, arbitrary 2D geometries of optical tweezer arrays can be generated [10]. Unfortunately, the

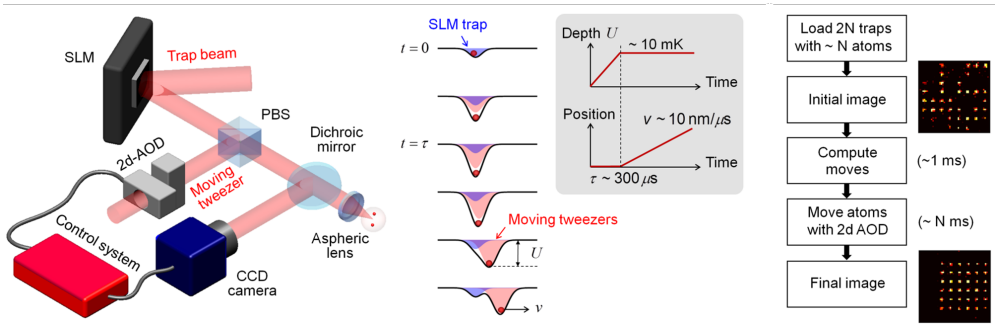

Figure 1.4. Schematic representaion of optical tweezers creation, loading and rearrangement using orthogonal AODs and SLM. The fixed tweezer array generated by SLM can be rearranged using the AODs.Fig. from Ref. [11].

phase patterns of a SLM cannot be reconfigured at sufficient speeds to engineer a defect-free array from the initial stochastic loading process. As a solution, one can combine a fixed arbitrary SLM array with a set of moving optical tweezers, generated by orthogonal AODs, which can pick and move atoms throughout the fixed array generated by the SLM. Thus, after an initial image of the stochastically loaded fixed array is taken, a series of moves can be programmed for the moving tweezers to move atoms into the desired configuration for a defect-free array in the fixed SLM geometry [11] as shown in Fig. 1.4.

1.3 Feedback control systems

Feedback control systems are widely used in experimental physics to maintain a measured quantity at a desired reference (setpoint) despite disturbances and parameter drifts [12]. In this thesis feedback loops are used, for example, to stabilize laser frequency and intensity. Defining the error signal as the difference between output (stabilized quantity) and input (setpoint) $e(s) = y(s) - r(s)$, the purpose of a feedback control loops is to implement some operational blocks that tend to minimize the error signal received as an input. A feedback control loop typically contains: a *sensor* that measures the controlled quantity, a *controller* that computes the control action based on the error between the measurement and the setpoint, an *actuator* that applies the control action to the system (plant), and possible dynamics and delays in each block. A minimal closed-loop structure is shown in Fig. 1.5.

Mathematically, using Laplace transforms the closed-loop transfer function from reference $r(s)$ to output $y(s)$ is:

$$T(s) = \frac{y(s)}{r(s)} = \frac{G_c(s)G_p(s)}{1 + G_c(s)G_p(s)H(s)}, \tag{1.21}$$

where $G_c(s)$, $G_p(s)$ and $H(s)$ denote the controller, plant and sensor transfer functions respectively. Stability and performance are determined by the open-loop $L(s) = G_c(s)G_p(s)H(s)$: margins (gain/phase), bandwidth, and disturbance rejection follow from the frequency response of $L(i\omega)$ where the dependence on the angular frequency has been made explicit as $s = i\omega$.

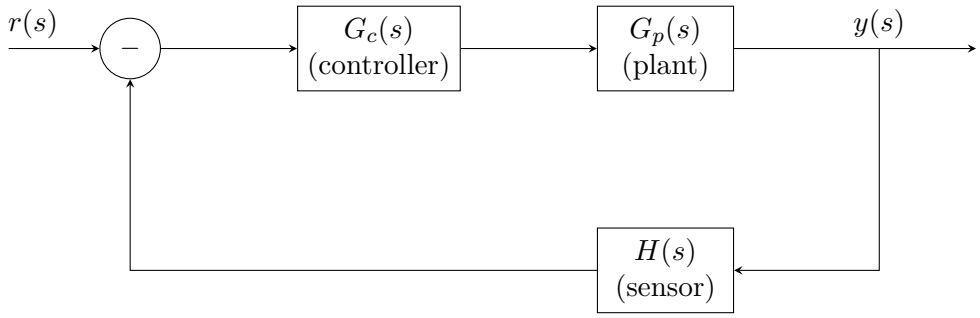

Figure 1.5. General single-loop feedback control architecture.

1.3.1 PID

Despite the advancing laser technology (both in stability, power and linewidth), there is alway the need for a stabilization in frequency or power when considering atomic physics application. In fact, experimentalists often find themselves in the situation of having to address specific atomic transitions with linewidths that can be very low, even mHz magnitude. Hence, the need to stabilize lasers using feedback control systems and, in particular, PIDs. Here, as it will be seen in the following parts of the thesis, the reference for the locking of laser frequency can have different natures: a specific transition of the atom observed via laser spectroscopy, a beatnote signal with another laser or the absorption peaks of an optical cavity. The Proportional–Integral–Derivative (PID) controller is the most widely used feedback controller in experimental setups because of its simplicity and effectiveness for a broad class of systems. In the time domain the PID output can be written as:

$$u(t) = K_P e(t) + K_I \int_0^t e(\tau)\, d\tau + K_D \frac{de(t)}{dt}, \tag{1.22}$$

where $e(t) = r(t) - y(t)$ is the control error, K_P the proportional gain, K_I the integral gain and K_D the derivative gain. In parallel (Laplace) form the controller transfer function is

$$G_c(s) = K_P + \frac{K_I}{s} + K_D s. \tag{1.23}$$

An alternative, commonly used parametrization (series form) is

$$G_c(s) = K_P \left(1 + \frac{1}{T_I s} + T_D s\right), \tag{1.24}$$

with $T_I = K_P/K_I$ the integral time constant and $T_D = K_D/K_P$ the derivative time constant.

The parameters K_P, K_I, K_D are all tunable and have to be adjusted in a way that ensures the control loop output is both stable enough and fast enough at the same time. In particular, they can be interpreted in the following way:

- *Proportional* (K_P) gives an immediate control action proportional to the error; larger K_P increases bandwidth but may induce oscillations.
- *Integral* (K_I) eliminates steady-state error (offset) by accumulating the error; it improves low-frequency disturbance rejection but reduces phase margin and can introduce windup if the actuator saturates.
- *Derivative* (K_D) provides anticipatory action based on the error slope; it increases damping and improves transient response but is sensitive to measurement noise.

As already mentioned before, the parameters have to be tuned to grant the best possible functioning of the PID control.

Two commonly used methods (and the ones used in this thesis) are:

- *Manual*: A usual algorithm used for simplicity in tuning a PID control loop is: start by turning up the proportional gain until the system oscillates, then turn down the gain until the oscillations are almost suppressed; add integral gain to eliminate setpoint droop (with the proportional gain only, the steady state error tends to an offset), and turn down the proportional gain a bit more to offset the destabilizing lag of the integral term; lastly, in case it is needed (for the uses of this thesis it does never make a difference), add a derivative term.
- *Ziegler–Nichols* [13]: increase K_P until the loop oscillates (ultimate gain K_u) with period T_u. Then set gains according to the classical table (for a PID): $K_P \approx 0.6K_u$, $T_I \approx 0.5T_u$ and $T_D \approx 0.125T_u$. These values are aggressive and often require refinement.

In the context of laser frequency or intensity stabilization (e.g. using an actuator such as a piezo on a cavity mirror or an AOM drive amplitude), the PID roles are:

- K_P: reduces immediate frequency deviation and increases lock bandwidth.
- K_I: compensates slow drifts (thermal, mechanical) and removes steady offset between laser and reference.
- K_D: damps oscillations introduced by actuator or plant resonances, i.e. K_D will often not be needed for the specific applications shown in this this thesis.

Further details on laser-specific implementations are discussed in the next chapter.

1.4 Pound–Drever–Hall technique

In laser frequency stabilization it is common to use optical cavities (or nowadays ultra-stable cavities) as a reference for frequency stabilization. In fact, cavities work as 'filters' in the frequency domain: they have resonance frequencies evenly spaced by a quantity called free spectral range:

$$\nu_n = n \cdot \nu_{FSR} \tag{1.25}$$

where ν_n are the resonance frequencies of the optical cavity, n is an integer number and ν_{FSR} is the free spectral range, which is given by:

$$\nu_{FSR} = \frac{c}{2L} \tag{1.26}$$

where c is the light speed in vacuum and L is the length of the optical cavity. A Fabry-Perot cavity transmission signal is shown In Fig. 1.6.

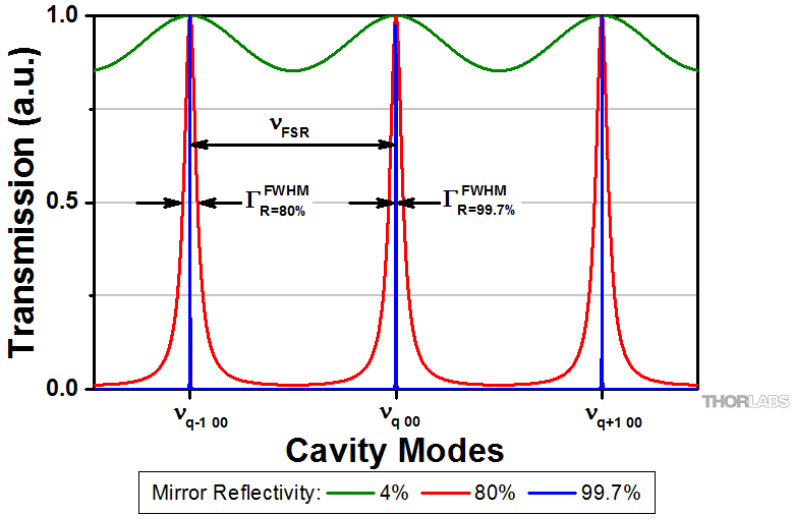

Figure 1.6. Example of a Fabry-Perot cavity transmission signal. ν_{FSR} is the free spectral range, while Γ^{FWHM} is the full-width at half-maximum linewidth of the transmission peaks and it depends on the reflectivity as shown.
Fig. from `https://www.thorlabs.com/newgrouppage9.cfm?objectgroup_id=9021`

This means that, in reflection, by sweeping the frequency of the laser some absorption peaks are observed at the cavity resonance frequencies. One could use a peak of the cavity as reference, but, since peaks are symmetrical, just looking at the signal there is no way to differentiate if the laser is moving to higher or lower frequencies with reference to the resonance one, thus, it is impossible to bring the laser back. To overcome this problem, the next step is to generate a derivative signal through a frequency modulation and demodulation of the laser. This way, if the frequency of the laser moves towards lower values, the signal will decrease or increase (depending on the phase of the demodulation), while in the opposite case, also the signal will do

the opposite, allowing for the differentiation between the two cases (see Fig. 1.7).

Pound–Drever–Hall (PDH) locking is a robust and high-bandwidth method to do exactly that [14, 15]. Using this technique the phase (rather than the power) of the light reflected from a reference cavity can be measured by creating radiofrequency phase sidebands onto the incident beam and demodulating the photodetector signal at the modulation frequency. In the next sections, the scheme (presented in Fig. 1.8) and the details to implement the PDH technique are thoroughly explained.

1.4.1 Principle

The basic idea is to send a phase-modulated laser beam onto a Fabry–Pérot cavity and detect the reflected light. Near resonance the reflected field (from the input mirror) and the leakage field (from the intra-cavity standing wave) have nearly equal amplitudes but a frequency-dependent relative phase; this phase difference is the quantity that tells us whether the laser is above or below cavity resonance. By beating the reflected carrier with phase sidebands (created before the cavity) and demodulating at the modulation frequency, one obtains a zero-crossing error signal that is antisymmetric about cavity resonance and therefore suitable for feedback.

1.4.2 Quantitative model

We denote the reflection coefficient of the cavity by $F(\omega)$ (ratio of reflected to incident field amplitudes at the angular frequency ω of the laser beam). Phase modulation at frequency Ω with modulation amplitude β produces first-order sidebands at $\omega \pm \Omega$. Writing the incident field including first-order sidebands,

$$E_{\text{in}}(t) \approx E_0\big[J_0(\beta)e^{i\omega t} + J_1(\beta)e^{i(\omega+\Omega)t} - J_1(\beta)e^{i(\omega-\Omega)t}\big],$$

where J_0 and J_1 are the zero and first order Bessel functions. The reflected field is obtained by multiplying each spectral component by the cavity reflection coefficient at the corresponding frequency and summing. The reflected optical power contains components oscillating at Ω (and 2Ω) that come out calculating $I_{rif} \propto |E_{rif}|^2$, and it is the Ω-component that carries the phase information of the reflected carrier. Mixing the photodiode output with the local oscillator at Ω and low-pass filtering yields the *error signal* e.

In the regime typically used for cavity locking (carrier near resonance, sidebands off resonance), the demodulated error signal is linear to first order around resonance and can be written in the compact form

$$e(t) \simeq \mathcal{D}\,\Delta f(t), \tag{1.27}$$

where Δf is the frequency deviation of the laser from the cavity resonance and $\mathcal{D}$ is the *frequency discriminant* (slope of the error signal, units V/Hz if e is in

volts). The discriminant depends on the optical powers in carrier and sidebands, the cavity linewidth, the photodetector gain and mixer gain. For practical purposes one treats $\mathcal{D}$ as the calibration factor that converts the measured servo error voltage into an equivalent frequency offset.

1.4.3 Modulation frequency and regimes

Two useful regimes are often distinguished:

- *Low modulation frequency* (Ω small compared to the cavity linewidth): the error signal corresponds intuitively to the derivative of the reflected power with respect to frequency (adiabatic picture) as shown in Fig. 1.7a.
- *High modulation frequency* (Ω large compared to the cavity linewidth, but small compared to the free spectral range): the sidebands are essentially totally reflected while the carrier probes the resonance; the demodulated signal is proportional to the imaginary part of $F(\omega)$ and is linear near resonance. This high-Ω regime is widely used because it decouples the measurement from slow cavity build-up dynamics and generally yields higher servo bandwidth. An example signal is shown in Fig. 1.7b.

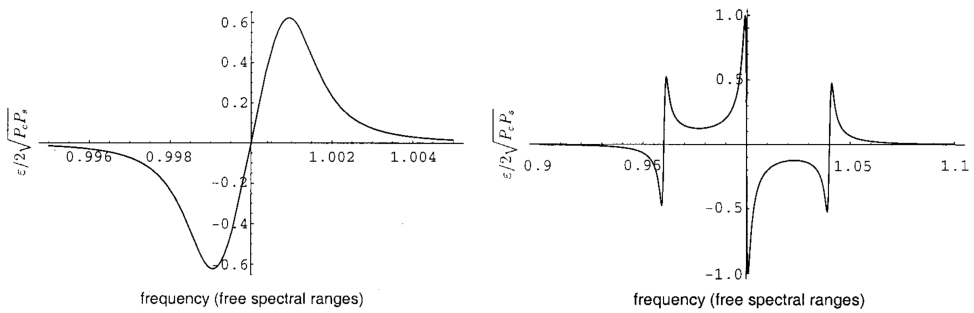

(a) Low modulation frequency signal. From Ref. [15]

(b) High modulation frequency signal. From Ref. [15]

Figure 1.7. (a) The Pound–Drever–Hall error signal, $\frac{\epsilon}{2\sqrt{P_c P_s}}$ (P_c is the power of the carrier while P_s is the power of the sidebands) versus $\frac{\nu}{\Delta\nu_{FSR}}$, for the case when the modulation frequency is low. Here, the modulation frequency is about half a linewidth. (b) The Pound–Drever–Hall error signal, $\frac{\epsilon}{2\sqrt{P_c P_s}}$ versus $\frac{\nu}{\Delta\nu_{FSR}}$, for the case when the modulation frequency is high. Here, the modulation frequency is about twenty linewidths.

1.4.4 Implementation

A compact sketch of optical and electronic parts needed to implement PDH technique is given in Fig. 1.8.

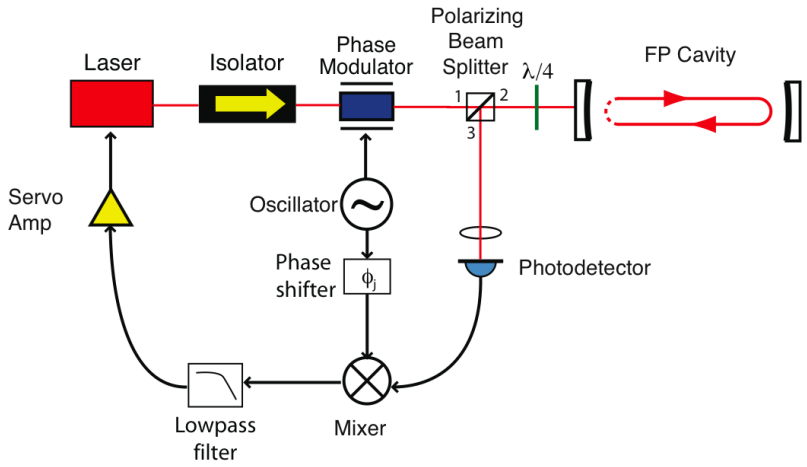

Figure 1.8. The basic layout for locking a cavity to a laser. Red line is the laser beam, while black line is the electronic part. The signal going to the laser controls its frequency.

A standard implementation contains:

1. An electro-optic phase modulator (EOM / Pockels cell) driven by an rf oscillator at Ω (the local oscillator, LO).

2. An optical isolator (polarizing beam splitter (PBS) + quarter waveplate) and the reference Fabry–Pérot cavity.

3. A fast photodetector that measures the reflected beam. The detector bandwidth must cover Ω and its harmonics.

4. An rf mixer which multiplies the photodiode signal by the LO. A phase shifter in the LO path is used to set the demodulation phase (necessary to obtain the correct quadrature and the canonical antisymmetric error signal).

5. A low-pass filter after the mixer to remove the connected time-dependent part of the signal at frequency 2Ω and higher components and produce the error signal for the servo.

6. A servo controller (PID or more advanced) that filters/amplifies the error and drives the laser actuator (piezo, current, AOM) to correct frequency errors.

PDH technique was classically introduced for frequency locks that use an optical cavity signal as reference but it is not necessary. Any signal that presents peaks can be modulated and used as a reference for the Pound-Drever-Hall technique; the only necessary characteristic for ta signal to be used as reference

is that it is stable enough for the application we need.
As we will see in chapter 4, in this thesis different signals have been used as reference for PDH, i.e. the Ytterbium spectroscopy signal or the beatnote between the laser that has to be locked and another reference laser, already locked on the frequency needed.

Chapter 2

Experimental setup project

In the following chapter, the planned experimental setup is described, with the aim of providing a clear understanding of the reason behind the steps carried out during the thesis work. In particular, the fundamental elements necessary to understand how a quantum computing platform is implemented using atoms will be introduced, from qubits to single- and multi-qubit gates.

2.1 Ytterbium

The fundamental ingredient of a quantum computer is the qubit: a two-level quantum system on which all computational operations (gates) are performed. In the case of neutral atoms platforms, the qubit consists of two long-lived internal states of the atoms, chosen in such a way to ensure long coherence times.

In this experiment, the candidate chosen to perform such a role is ^{171}Yb. This isotope has been selected due to several favorable properties, compared to more commonly used alkaline atoms, that make it especially well-suited for quantum information processing:

- The ground state of ^{171}Yb has total electronic angular momentum $J = 0$ and nuclear spin $I = \frac{1}{2}$, which results in a two-level system formed by two Zeeman sublevels $|m_I = -\frac{1}{2}\rangle \equiv |0\rangle$ and $|m_I = \frac{1}{2}\rangle \equiv |1\rangle$ (Fig. 2.1) that are highly insensitive to stray magnetic fields. The reason behind this is that when one calculates the Zeeman shift of the energy level in absence of total angular momentum ($J = 0$), it is given by: $\Delta = g_I \mu_N m_I B$ where $\mu_N = \frac{e\hbar}{2m_p}$ is called nuclear magneton. It differs from the Bohr magneton just by the electron mass m_e factor, that is substituted by the proton mass m_p. Thus $\frac{\mu_B}{\mu_N} = \frac{m_p}{m_e} = 1836$, meaning that nuclear spin Zeeman sublevels are 3 orders of magnitude less sensitive to variations in the magnetic field with respect to hyperfine structure Zeeman sublevels. These features make these sublevels ideal for encoding robust qubits.

- Its atomic structure, similar to that of alkaline-earth atoms, features both broad and narrow optical transitions. These transitions are both important for several reasons. They allow for efficient laser cooling to

microkelvin temperatures through Zeeman slowing on the broad 399 nm $^1S_0 \rightarrow {}^1P_1$ transition ($\Gamma \simeq 29.1$ MHz) followed by magneto-optical trapping on the narrow 556 nm $^1S_0 \rightarrow {}^3P_1$ transition ($\Gamma \simeq 182$ KHz) and they can both be used for detection, in particular the broad transition can be used for fast imaging of the atoms, while the narrow transition can be used for slow, nondestructive imaging of the qubit state. It is important to notice that, in this case, "nondestructive measurement" just means that the atom are not pushed out of the trap because of the low energy of the radiation and the low photon scattering rate of the transition, but the state still loses its coherences.

- The presence of a metastable clock state ($^3P_0$), which also has J=0, enables the encoding of two distinct, long-lived qubits within a single species. This feature opens the possibility for advanced quantum error correction protocols, in which one atom in the clock state acts as qubit, while several others in the ground state are used as ancillas.

- The clock state also offers the advantage of single-photon excitation to Rydberg states, resulting in higher Rabi frequencies and no off-resonant scattering from intermediate states, in contrast to the two-photon excitations usually employed in alkaline species.

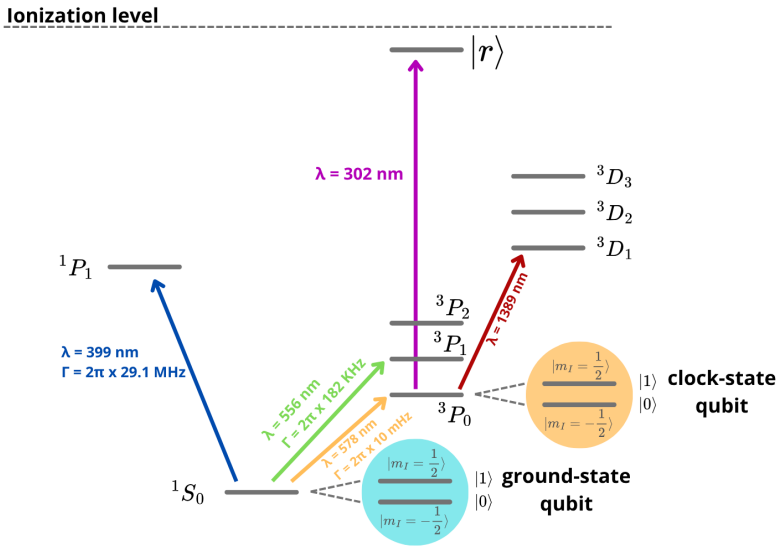

Figure 2.1. Schematic representation of main Yb levels and transitions. The two candidates to be good qubits are highlighted in light blue and yellow.

2.2 Atom cooling stages

In order to arrive at a functioning platform where single atoms are trapped in optical tweezers and can be manipulated, several atom cooling stages are needed.

In fact, initially, just a cloud of hot atoms is produced inside an oven in a vacuum chamber, starting from a solid piece of Ytterbium. The heat from the oven makes Ytterbium atoms evaporate from the solid piece. Right after the oven, a small aperture that lets atoms pass through and selects the direction of their velocities is present. Hence the atoms are now collimated into a hot atomic beam with high velocity (depending on the temperature of the oven) that needs to be slowed down and captured.

The cooling stages needed for Ytterbium and in particular for this experiment have been explained in chapter 1 and they are:

1. *Zeeman slower*: an initial slowing stage is carried out by a Zeeman slower (discussed in section 1.1.1). It exploits the $^1S_0 \rightarrow ^1P_1$ transition to slow the atoms down from $\simeq 310$ m/s (estimated on the base of oven temperature and Ytterbium atomic mass) to 40 m/s.

2. *2D MOT* (section 1.1.2): Since right after the oven the atomic beam needs to be redirected through a small hole into a vacuum pumping chamber and then into a glass cell, a 2D MOT is implemented to deflect the beam. The MOT, combined with the Zeeman slower, is able confine the beam transversely and redirect into the glass cell where the experiment will take place.

3. *Angle slowing*: The capturing step of the atomic beam consists of a 3D green MOT performed on the $^1S_0 \rightarrow ^3P_1$ transition, which has a capture velocity of few m/s. This means that the velocity reached by the first two cooling steps is not small enough. This is why an angle slowing stage is implemented in the glass cell with two inclined beams that again address the $^1S_0 \rightarrow ^1P_1$ transition in order to reach the capture velocity of the 3D MOT:

4. *3D MOT*: after the angle slowing, a 3D MOT is implemented on the $^1S_0 \rightarrow ^3P_1$ transition. The MOT role is to trap the atoms (average velocity is zero) and cool them down at the same time. The Doppler temperature of the green transition is $\sim 1\ \mu$K, which is the temperature reached by the optical molasses. This step is very important, because the atoms reach temperatures of some orders of magnitude below the initial frequency trap of the tweezers, which is $\sim 1\ m$K.

All these cooling stages are schematically represented in Fig. 2.2

After all these steps of cooling, the atoms are ready to be trapped in optical tweezers. The traps are switched on and the MOT is switched off. The atoms lifetime in tweezers is limited by collisions with free atoms in the chamber, and it is around seconds to tens of seconds, but under cryogenic environment it can be extended up to hours. In the case of this experiment, tweezers will be kept at room temperature, but it won't be a limit because quantum computational tasks don't exceed milliseconds scale.

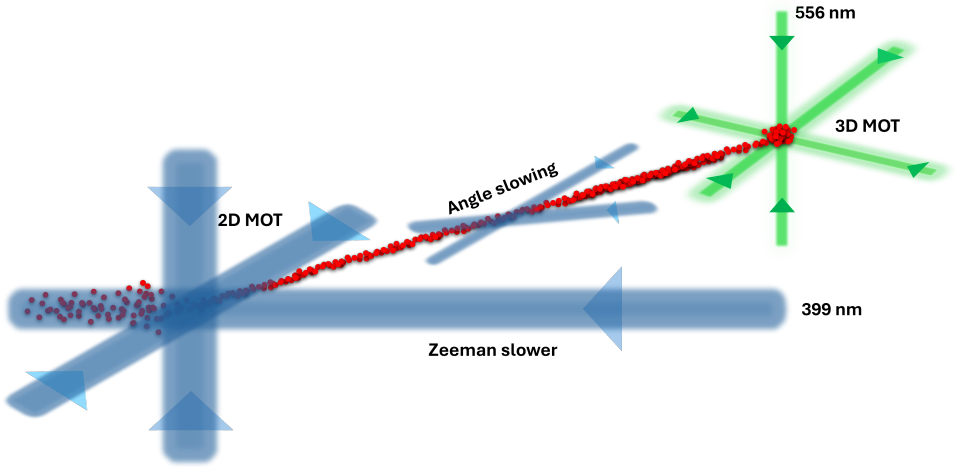

Figure 2.2. schematic representation of all the cooling stages implemented on the atoms.

2.3 Rydberg atoms

One of the most challenging aspects of neutral atoms platforms is enabling the interactions between atoms in different tweezers. That is, because neutral atoms interact via short-range van der Waals interactions, which scale as $\frac{C_6}{r^6}$ where r is the interatomic distance and C_6 is the van der Waals coefficient, that strongly depends on the principal quantum number n of the interacting atoms. This means that over the distance between two tweezer traps (few micrometers) there's approximately zero interaction among atoms with low principal quantum number.

To solve this problem it is necessary to find a way to enable strong interactions between atoms in different traps and that is Rydberg atoms. Rydberg atoms are atoms excited to states with high principal quantum number $n \gg 1$, slightly below the ionization continuum. Many properties of Rydberg states scale strongly with n [16, 17], which makes these states useful tools for quantum engineering. Though this scaling is exact in Hydrogen, it is not quite right in multielectron atoms. In practice, the general scaling properties can be recovered by making a correction to n: $n^* = n - \delta$ where δ is called the quantum defect, and arises due to the interaction between the Rydberg electron wave function and the core. It is generally a function of n and angular momentum quantum numbers, though for large enough principle quantum number (such that the Rydberg wave function has little overlap with the core), it is roughly independent of n. The quantum defect correction allows the discussion of general scaling properties of Rydberg states as a function of n^*. Here is a table of the n^* scaling of the most relevant Rydberg state properties:

In particular, among these properties, the one that stands out the most is the fast increase of the short-range atom-atom Var der Waals interaction as n^{11}. As a result, two Rydberg atoms with $n > 50$ localized in two nearby optical

Parameter	x (n^{*x} scaling)
binding energy	-2
wavefunction radius	2
energy spacing between neighboring states	-3
wavefunction probability at core	-3
dipole matrix element to ground state	-3/2
radiative lifetime	3
dipole matrix element to neighboring state	2
blackbody radiation lifetime	2
DC stark shift	7
van der Waals interaction	11
resonant dipole-dipole interaction	4

Table 2.1. n^* scaling of the most relevant Rydberg state properties.

tweezers, separated by $r \simeq \mu$m can experience a substantial interaction energy exceeding the MHz scale. This strong interaction also leads to entanglement thanks to a phenomenon called Rydberg blockade [18].

The phenomenon comes from the fact that when the two atoms are interacting, the system has to be described with collective states. Let us describe each atom as a two-level system, where $|g\rangle$ is the ground state and $|r\rangle$ is a Rydberg state, and consider a laser resonant with the $|g\rangle \rightarrow |r\rangle$ transition. Then, describing the system with collective states of the two interacting atoms and calculating the dipole-dipole interaction, one can derive a shift in the energy between $|gg\rangle \rightarrow |gr\rangle$ and $|gr\rangle \rightarrow |rr\rangle$, as shown in Fig. 2.3. This means that if two interacting atoms are both in the ground state and are shined by the same laser, only one of them will be excited, leading to an entangled state $|\psi\rangle = \frac{1}{\sqrt{2}}\Big(|gr\rangle + |rg\rangle\Big)$.

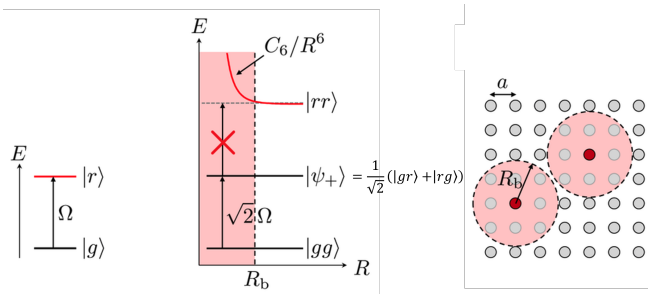

Figure 2.3. Mechanism of the Rydberg blockade. We consider a two-level system with states $|g\rangle$ and $|r\rangle$ coupled coherently with Rabi frequency Ω. Within a certain radius that we called R_b the two atoms in state $|rr\rangle$ interact strongly due to the extended Rydberg wavefunction; consequently the $|gr\rangle \rightarrow |rr\rangle$ transition is shifted with respect to the $|gg\rangle \rightarrow |gr\rangle$ transition. This enables the so called Rydberg blockade, e.g. two atoms with a relative distance $< R_b$ can not get simultaneously excited to the Rydberg state.

2.4 Quantum gates

To actually perform quantum computing, one needs to design a set of operations in order to manipulate the quantum information stored in their states [19]. In particular, it is necessary to be able to implement:

- single-qubit gates
- multi-qubit gates

2.4.1 Single-qubit gates

quantum mechanical description of a two-level system is often given using a particular representation, called Bloch sphere, shown in Fig. 2.4.

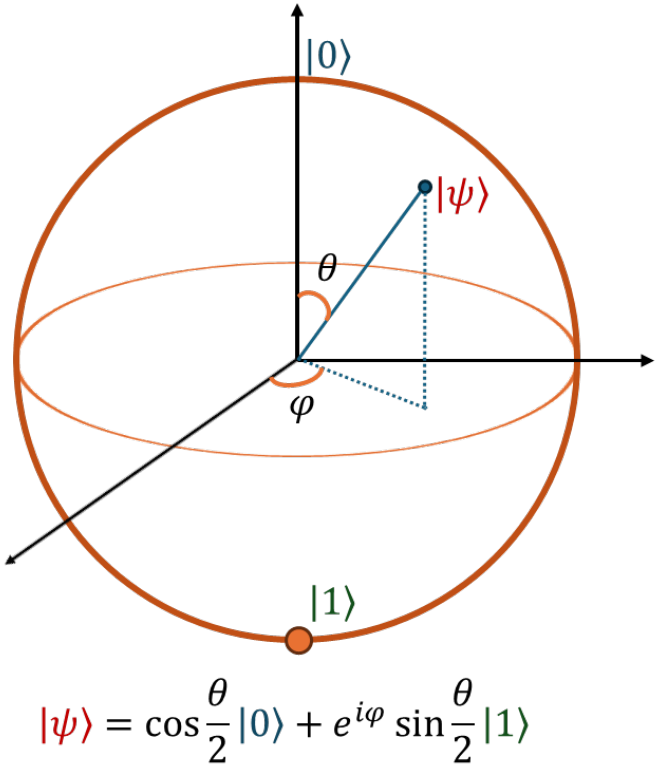

Figure 2.4. Bloch sphere. Usual representationn of a two-level system in quantum mechanics, and in particular in quantum information.

Here the state is represented as a point on a sphere, where the two poles are the $|0\rangle$ and $|1\rangle$ states of the qubit and the general qubit state can be written as:

$$|\psi\rangle = \cos\tfrac{\theta}{2}\,|0\rangle + e^{i\varphi}\sin\tfrac{\theta}{2}\,|1\rangle \tag{2.1}$$

Any possible operation on the qubit can be represented as a movement of a point over the Bloch sphere. Single-qubit gates are simply this, an arbitrary

operation on the qubit, i.e. an arbitrary 3D rotation over the Bloch sphere, as illustrated in Fig. 2.5.

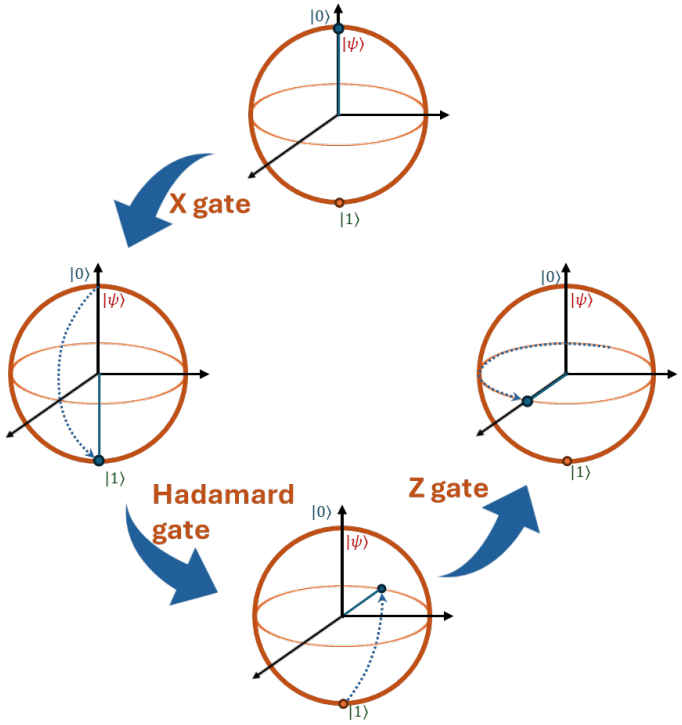

Figure 2.5. Schematic illustration of single qubit gates as rotations on the Bloch sphere. Just three example gates are shown: X gate, Hadamard gate and Z gate.

Typical single-qubit gates are the Pauli gates, whose action is represented by the matrices:

$$X = \begin{pmatrix} 0 & 1 \\ 1 & 0 \end{pmatrix} \tag{2.2}$$

$$Y = \begin{pmatrix} 0 & -i \\ i & 0 \end{pmatrix}$$

$$Z = \begin{pmatrix} 1 & 0 \\ 0 & -1 \end{pmatrix}$$

and the Hadamard gate:

$$X = \frac{1}{\sqrt{2}} \begin{pmatrix} 1 & 1 \\ 1 & -1 \end{pmatrix} \tag{2.3}$$

often used in combination with a controlled-NOT gate (it will be explained in the following section) to reach a Bell state starting from a quantum two qubit initialized in $|0\rangle$.

Single-qubit gates implementation with neutral atom qubits is particularly straightforward via Raman transitions. Specifically, in this project we reference to the technique used in [20] to implement fast arbitrary single-qubit gates on the ground-state qubit. Here we recall that the logical basis is encoded in the two Zeeman sublevels of $^1S_0$, i.e. $|0\rangle : m_F = +\frac{1}{2},\ |1\rangle : m_F = -\frac{1}{2}$.

The scheme is illustrated in Fig. 2.6. Here, Raman transitions are driven by two beams that have different purposes. Let's name them X and Z. In presence of a magnetic field $\vec{B}$ that defines the quantization axis, both the $^1S_0$ state (qubit) and $^3P_1$ state (intermediate level for the Raman transition) are split into Zeeman sublevels. The X beam has linear polarization, tilted by an angle with respect to the quantization axis, meaning that it drives excitation with $\Delta m = \pm 1, 0$. In the atoms reference frame, the beam has two polarization components, one linear π and on circular σ. Rabi oscillations are driven in the regime where $\Omega_X \gg \Delta_N$ where Ω_X is the Rabi frequency of the interaction of the atoms with the X beam and Δ_N is the Zeeman energy splitting of the ground state. The detuning Δ_X of the beam from $^3P_1$ is much greater than the splitting of the state. In this regime, the Rabi frequency depends on the relative phase ϕ of the two components of the X beam as:

$$\Omega_X \simeq \Omega_\sigma \Omega_\pi \frac{\cos\phi}{\Delta_X} \tag{2.4}$$

where the ratio of the coupling strengths Ω_σ and Ω_π is fixed by the ratio between the two components electric fields E_z and E_y. This particular beam geometry is symmetrical with respect to the two components of the circular polarization σ^+ and σ^-, meaning that the magnitudes of the two components $|\Omega_{\sigma^\pm}| \equiv \Omega_\sigma$ are equal. In this regime, a single beam can drive Raman transitions simultaneously through the two separate pathways, albeit with a small detuning given by the qubit splitting. Therefore, the X beam drives population inversions between $|0\rangle$ and $|1\rangle$, but it doesn't change the relative phase between the two qubits.

Given a qubit in a superposition state $|\psi\rangle = \cos\frac{\theta}{2}|0\rangle + e^{i\varphi}\sin\frac{\theta}{2}|1\rangle$, relative phase φ variations are driven by the free evolution of the system and the speed of this variations depends on the energy splitting between the two levels of the qubit. The Z beam is introduced to accelerate phase rotations. When X beam is switched off, Z doesn't drive excitations because it is just σ_+ polarized,

but it induces a differential light shift on the qubit that increases the splitting, Hence accelerating the increase rate of the relative phase. A scheme of this gate architecture is presented in Fig. 2.6.

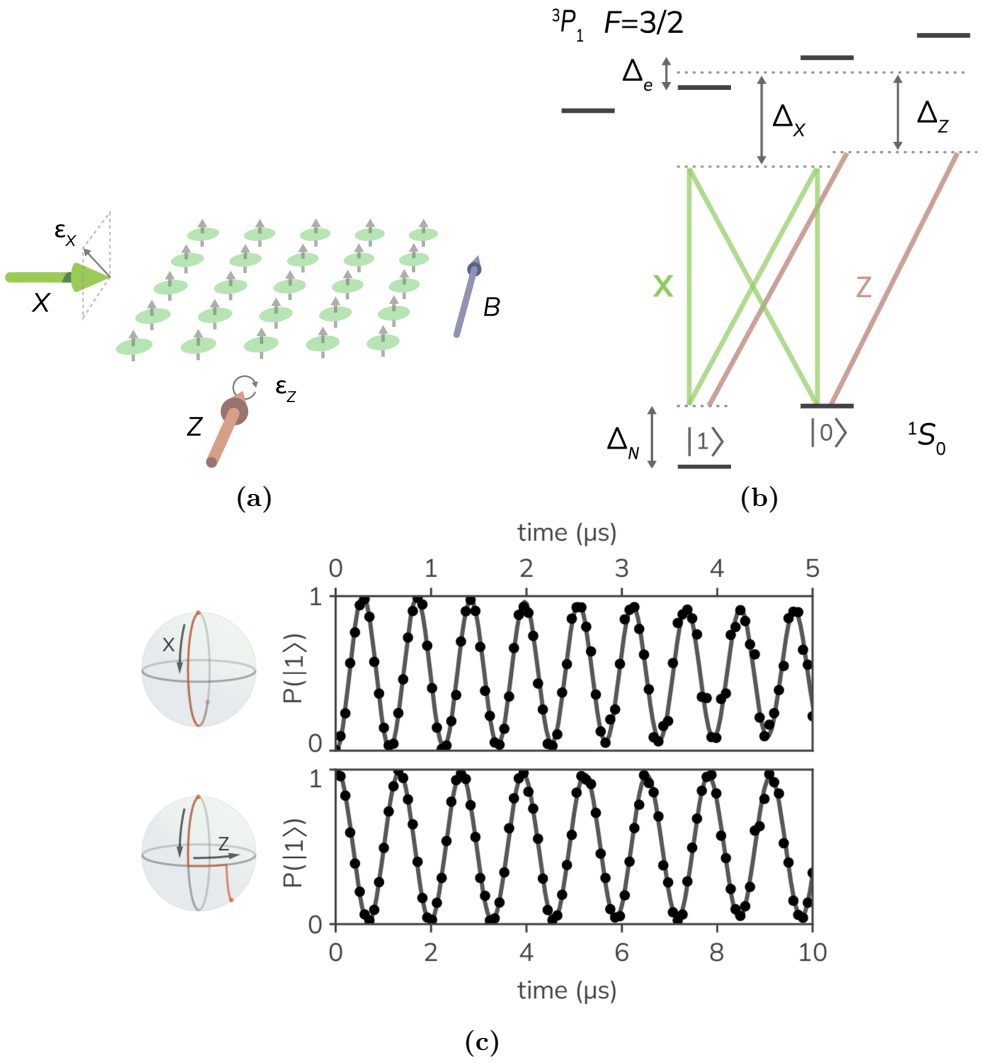

Figure 2.6. Single-qubit gate implementation via Raman transitions. (a,b) Raman transitions between $|0\rangle$ and $|1\rangle$ are mediated by a single beam (X in figure), whose polarization is linear but inclined with reference to the quantization axis, defined by the direction of the magnetic field $\vec{B}$. Z is a σ^+ polarized beam along the quantization axis and it is used to control light shift, mainly to increase the energy difference between the two qubits and consequently induce faster relative phase shifts. (C) Gate duration is shown, both for X induced and Z induced gates the duration is on the order of the microsecond. Figures from Ref. [20]

2.4.2 multi-qubit gates

Multi-qubit gates are much more difficult to be implemented than single-qubit gates, because interactions between different atoms that lead to entanglement are needed. At present there are mainly three established methods to create entangling gates using Rydberg blockade [21, 22, 23]; here, only the most straightforward method is presented (for semplicity only the two-qubis gate case is described).

The fundamental two-qubit gate is the controlled-NOT (CNOT) gate, which is represented in matrix form as:

$$CNOT = \begin{pmatrix} 1 & 0 & 0 & 0 \\ 0 & 1 & 0 & 0 \\ 0 & 0 & 0 & 1 \\ 0 & 0 & 1 & 0 \end{pmatrix} \tag{2.5}$$

where the matrix is written on the computational two qubit basis $|00\rangle, |01\rangle, |10\rangle, |11\rangle$ and it is formed by two diagonal 2×2 block matrices, the first corresponding to the case of control qubit $c = 0$ and the second corresponding to $c = 1$. The CNOT gate can be obtained by a series of three easier gates: an Hadamard gate, a controlled-Z gate and another Hadamard gate, all three on the target qubit as shown in Fig. 2.7.

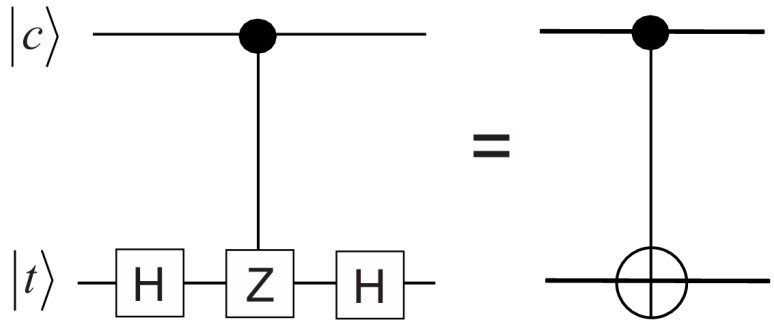

Figure 2.7. Representation of CNOT gate on quantum register.

Now lets see how to implement the CZ gate:

$$CZ = \begin{pmatrix} 1 & 0 & 0 & 0 \\ 0 & 1 & 0 & 0 \\ 0 & 0 & 1 & 0 \\ 0 & 0 & 0 & -1 \end{pmatrix} \tag{2.6}$$

Consider two qubit states $|0\rangle$ and $|1\rangle$, $|1\rangle$ is coupled to the Rydberg level $|r\rangle$ with Rabi excitation frequency Ω. The CZ gate is made up of three steps:

1. Control qubit is shined with a π pulse.
2. Target qubit is shined with a 2π pulse.
3. Control qubit is shined with a π pulse.

and it is illustrated in Fig. 2.8

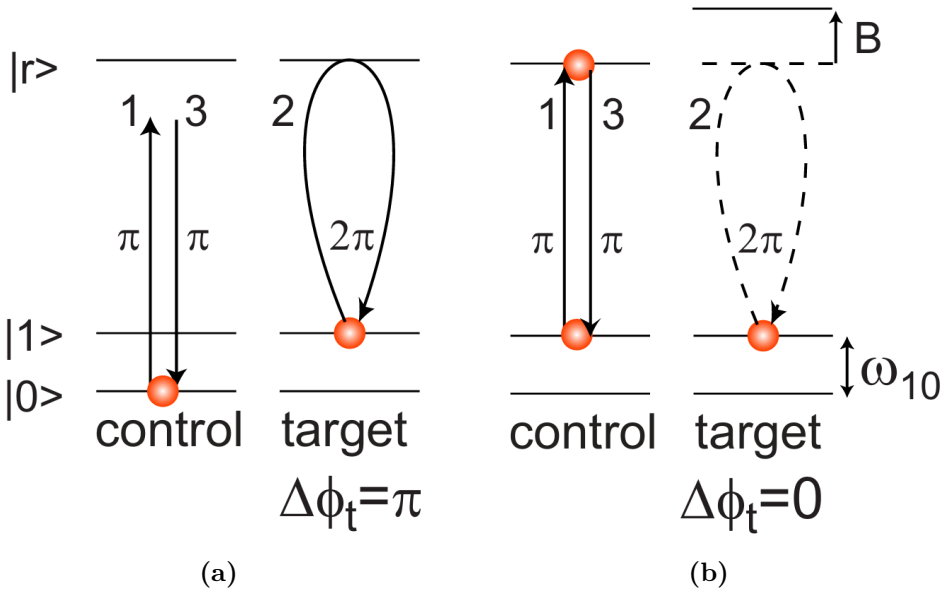

Figure 2.8. Rydberg-blockade controlled phase gate operating on input states (a) $|01\rangle$ and (b) $|11\rangle$. Quantum information is stored in the basis states $|0\rangle$, $|1\rangle$ and state $|1\rangle$ is coupled resonantly to a Rydberg level $|r\rangle$. The controlled phase gate is implemented with a three pulse sequence: (1) π pulse on control atom $|1\rangle \rightarrow |r\rangle$, (2) 2π pulse on target atom $|1\rangle \rightarrow |r\rangle \rightarrow |1\rangle$, and (3) π pulse on control atom $|r\rangle \rightarrow |1\rangle$. (a) Shows the case where the control atom starts in $|0\rangle$ and is not Rydberg excited, so there is no blockade. (b) Shows the case where the control atom is in $|1\rangle$, which is Rydberg excited, leading to blockade of the target atom excitation.

Analizing the four possible cases:

- Initial state is $|00\rangle$: neither the control or target qubit is coupled to the Rydberg state, hence the final state is $|00\rangle$
- Initial state is $|01\rangle$: control qubit is not coupled to $|r\rangle$, but the target qubit it is coupled, so it gets a phase shift of π due to the 2π pulse. The final state is $-|01\rangle$.
- Initial state is $|10\rangle$: same case as $|01\rangle$, but here the qubit coupled to $|r\rangle$ is the control qubit and the phase shift is caused by the two π pulses is again π. The final state $-|10\rangle$
- Initial state is $|11\rangle$: both qubits are coupled to $|r\rangle$, but after the first π pulse, the control qubit is in $|r\rangle$, so when the target qubit is shined with the 2π pulse, it is not excited due to Rydberg blockade. Finally the

second π pulse transfers the control state back to $|1\rangle$. The final state is $-|11\rangle$

This corresponds precisely to the action of a CZ gate except for a global phase term of $e^{i\pi}$.

2.5 The platform

To enable the implementation of gates and measurements on atomic qubits, the final setup will include several lasers at different wavelengths. A schematic representation is shown in Fig. 2.9.

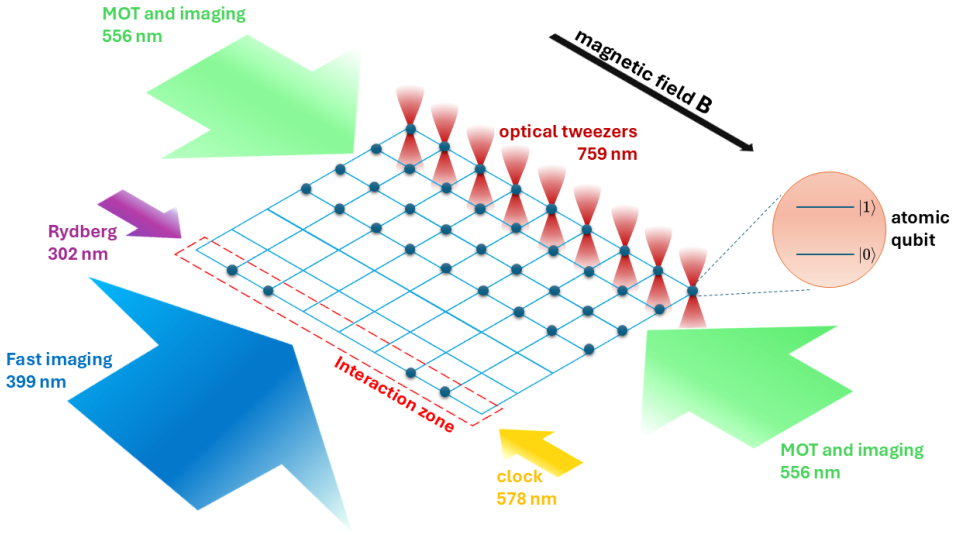

Figure 2.9. Schematic representation of the final designed setup. Here we show all the lasers used and their applications. We also show the particular advantage of this platform, which allows for both collective and selective excitations of qubits, allowing for very precise control of the platform.

The specific roles of the different wavelengths are as follows:

- *399 nm*: it is intensively used in the first phases of atoms cooling with different detunings to create a Zeeman slower, a 2D MOT and a final phase of angle slowing to reach the capture velocity of the subsequent 3D MOT created with the green 556 nm laser. It is also used when the atoms are already in the tweezers to do fast imaging, but with the disadvantage of it being destructive (it kicks atoms out of optical tweezers) because of its high energy and high photon scattering rate caused by the width of the transition.

- *556 nm*: it is used in the final part of the cooling to create a 3D MOT that, thanks to the very narrow transition ($\Gamma \approx 182$ KHz), can cool atoms down to microkelvin temperature. It is also employed for slow, nondestructive imaging of the atoms. Moreover, it is used to drive Raman transitions

between ${}^1S_0, |m = -\frac{1}{2}\rangle$ and ${}^1S_0, |m = \frac{1}{2}\rangle$, thereby implementing single-qubit gates on the ground-state qubit.

- *759 nm*: it is used for optical tweezers. The wavelength is chosen because it is magic for the ${}^1S_0 \rightarrow {}^3P_0$ transition as shown in Fig. 2.10. A magic transition is a transition where the states that are involved feel the same light shift from the laser exciting it, meaning their polarizability is the same.

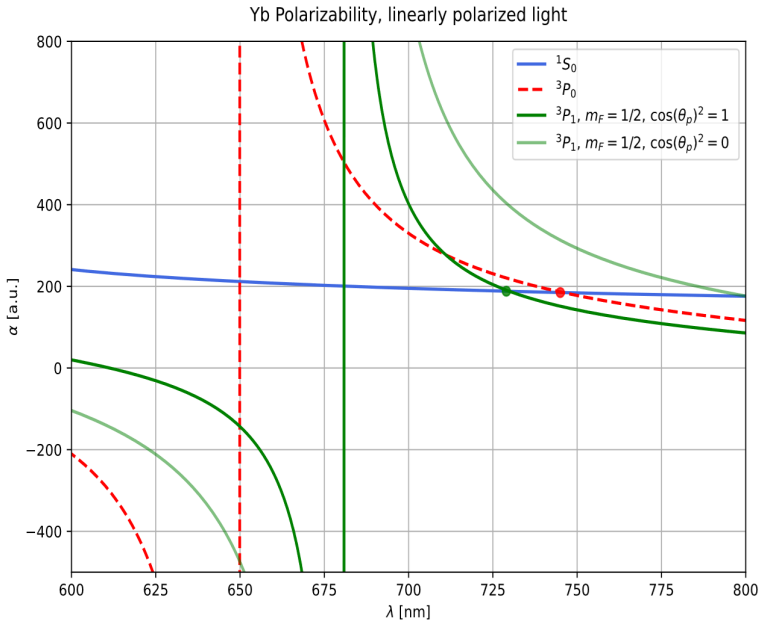

Figure 2.10. Yb polarizability as a function of the wavelength for both ${}^1\mathrm{S}_0$, ${}^3\mathrm{P}_1$ and ${}^3\mathrm{P}_0$ states. θ_p is the angle between the polarization of the beam and the quantization axis, that is needed to be considered for states with hyperfine total angular momentum $F \neq 0$, resulting in a non negligible component of tensor polarizability.

- *578 nm*: clock laser. It is used to coherently transfer the state of the qubit from the ground state to the clock state (${}^3\mathrm{P}_0$). This laser opens great variety of quantum computing applications, mainly for quantum error correction, where it is possible to use one of the two qubit states as ancilla and the other one as data.

- *302 nm*: Rydberg laser. It plays a fundamental role as it enables excitation from the ${}^3P_0$ state to a Rydberg state, thereby providing access to long-range interactions and, consequently, to the implementation of multi-qubit gates.

- *1389 nm*: This laser is employed for two distinct purposes. First, it can drive Raman transitions on the clock qubit (${}^3\mathrm{P}_0, |m = -\frac{1}{2}\rangle \rightarrow {}^3\mathrm{P}_0, |m = \frac{1}{2}\rangle$).

This type of platform offers several important advantages. The most remarkable is scalability: optical tweezers combined with spatial light modulators (SLMs) enable the creation of arbitrary arrays of atoms, whose size is limited only by technical factors such as the available laser power or the numerical aperture of the objective used to optically resolve the tweezers.

Another very advantageous feature, is the possibility to drive selective excitations. This means that through different techniques it is possible to excite selected atoms even shining all of them together. There are mainly two ways to enable selective excitations (Fig. 2.11a 2.11b):

1. adding another tweezer light at different wavelength on specific atoms to send them out of resonance through differential light shift;

2. changing the trap depth of specific tweezers to use their different motional states to send them out of resonance.

While the first technique is pretty clear in itself, let us shed some light on the second one. In this case, the idea is to use a long-lived state, which is dark to the interaction we want to drive ($^3P_0$ state in the case of Ytterbium and alkaline-earth atoms in general). Tweezers corresponding to atoms that have to be shielded from interaction, undergo a change in the trap frequency (just changing the intensity of the tweezer laser). This way we can drive frequency-selective motional sideband transitions exploiting the different shift in motional energy transitions due to the different trap frequencies. All the atoms excited to the dark state are now shelved from ground state transitions. This method has been demonstrated in Ref. [24].

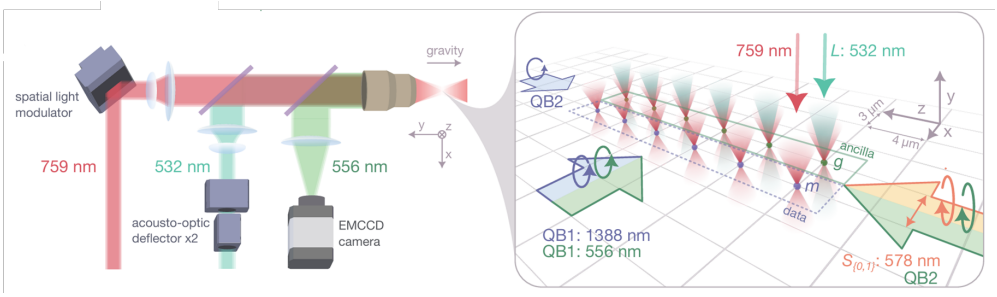

(a) Two different optical tweezers lasers ar used: one on all of the atoms, the second one just on selected ones. This way, the atoms shined by both feel a shift in their levels due to differential light shift caused by the second laser; meaning they are set out of resonance for the interaction lights used. From Ref. [25]

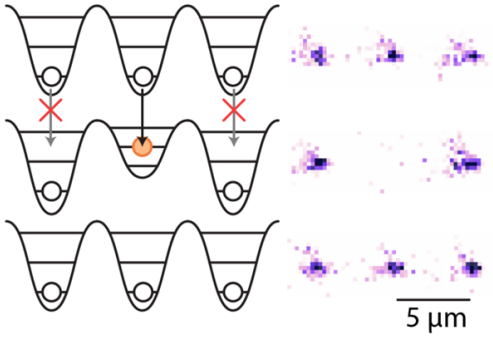

(b) Selected atoms are locally shelved via frequency-selective motional sideband driving to a long-lived dark state, meaning they are hidden from the chosen interaction. Here it is demonstrated by imaging three times (one each row) three atoms. In the second imaging (second row) the central atom is excited to the dark state. From Ref. [26]

Figure 2.11. Visual overview of techniques used to drive selective excitations.

Chapter 3

Vacuum system

This chapter will focus on the design and build up of the vacuum system where the whole experiment will take place. It consists of a commercial ytterbium atomic source (AOsense) connected to a pumping chamber and a science cell, as shown in Fig. 3.1.

Particular attention will be given to the specifications and purpose of each part of the vacuum system and to the ultra high vacuum techniques and procedures employed for their assembly.

Ultra high vacuum is a crucial point in the building of the experiment, and the whole functioning of the final setup depends on the order of magnitude of the vacuum that we will be able to reach in the chamber. There are many reasons behind the need for such a high vacuum system. Ultra-high vacuum (UHV) conditions are essential to ensure long trapping and coherence times. Poor levels of pressure inside the chamber strogly increase collisions between trapped atoms and background gas molecules, leading to heating and atom loss, that limit both the achievable temperature and the lifetime of the trap. Maintaining pressures below 10^{-9} mbar drastically reduces these collisions, allowing atoms to remain isolated for several seconds or even minutes. In the case of optical-tweezers experiments, UHV is therefore crucial to guarantee the stability of the trapped single atoms and to preserve the coherence required for quantum manipulations and gate operations, thus ensuring that computational time limiting factor is not caused by scattering events. Furthermore, UHV conditions minimize optical scattering and prevent the deposition of contaminants on optical surfaces such as viewports and mirrors, ensuring stable beam alignment and long-term optical performance of the setup.

3.1 General description of the system

A representation of the vacuum system is shown in Fig. 3.1, detailing each main component.

The AOsense chamber stores a solid Yb sample at its extremity. Here, there is an oven that heats the sample up to temperatures of ~ 400 °C, where the

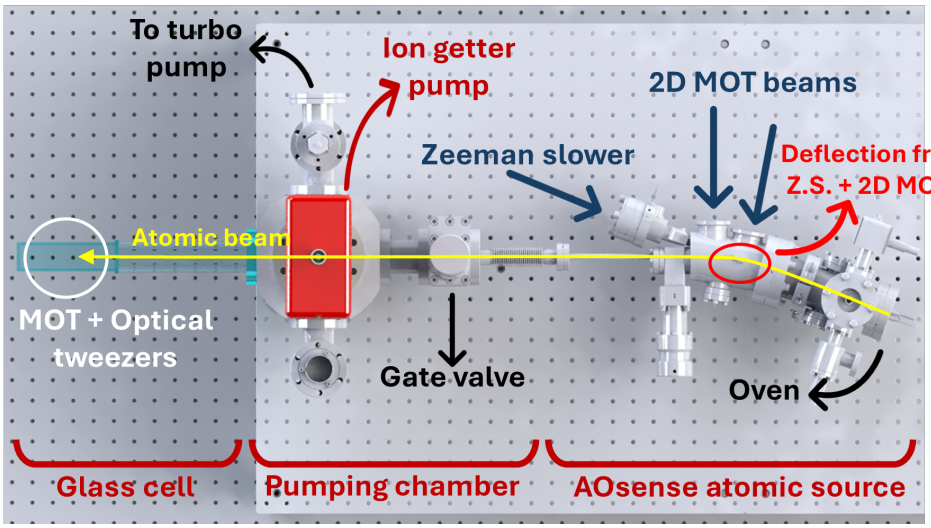

(a)

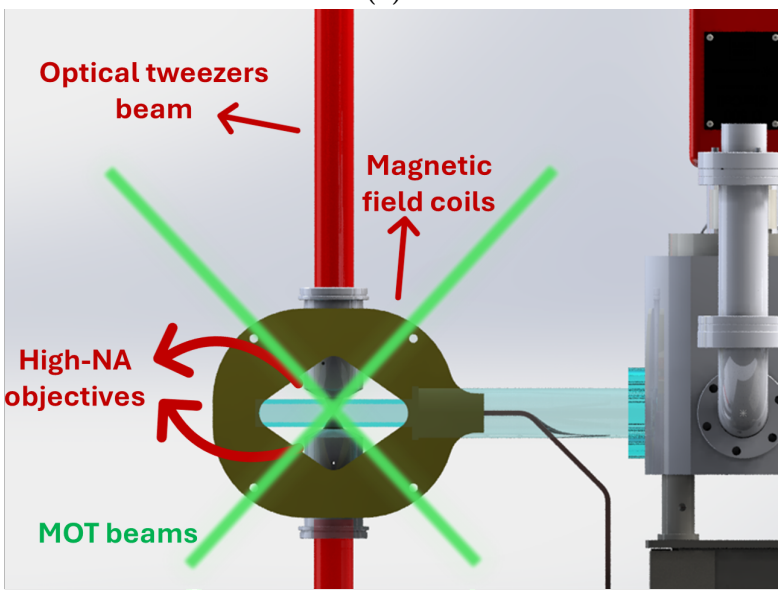

(b)

Figure 3.1. Design project of the vacuum system. (a) Top view of the vacuum system, consisting of an AO-sense chamber that houses the atomic source. An atomic beam is produced here, which is slowed and deflected through an initial Zeeman slowing stage followed by a 2D MOT, both operating at 399 nm. In the center, the SAES pumping chamber is visible, and on the left, the science cell, where the 3D MOT at 556 nm is implemented along with the optical tweezers at 759 nm.
(b) Side view, showing the high numerical aperture objectives used to generate optical tweezer arrays.

vapour pressure is high enough to have a Yb gas at a sufficiently high density for the experiment. The atoms, with now high kinetic energy, pass through an aperture that 'collimates' them into an atomic beam. Now the atoms need to be slowed down and their trajectory deflected in order to pass through the

pumping chamber and arrive in the glass cell. To do that, the AOsense chamber is equipped with two lateral windows (where two 2D-MOT beams are aligned), one window on the opposite extremity of the atomic source (for a Zeeman slower) and one window on top of the chamber (for laser spectroscopy). The main pumping chamber is equipped with a lateral flange that enables the connection to a turbo pump for a first rough pumping of the system. Furthermore, it is provided with an ion pump and a getter that were used in the final steps of the vacuum assembly. In the floowing, we go into detail of the two main vacuum chambers of the system and of the glass cell.

3.1.1 Atomic source

As it was already explained, the atomic source is a commercial one provided by AOsense. An image presenting all perspectives and pointing out all the components is shown in Fig. 3.2.

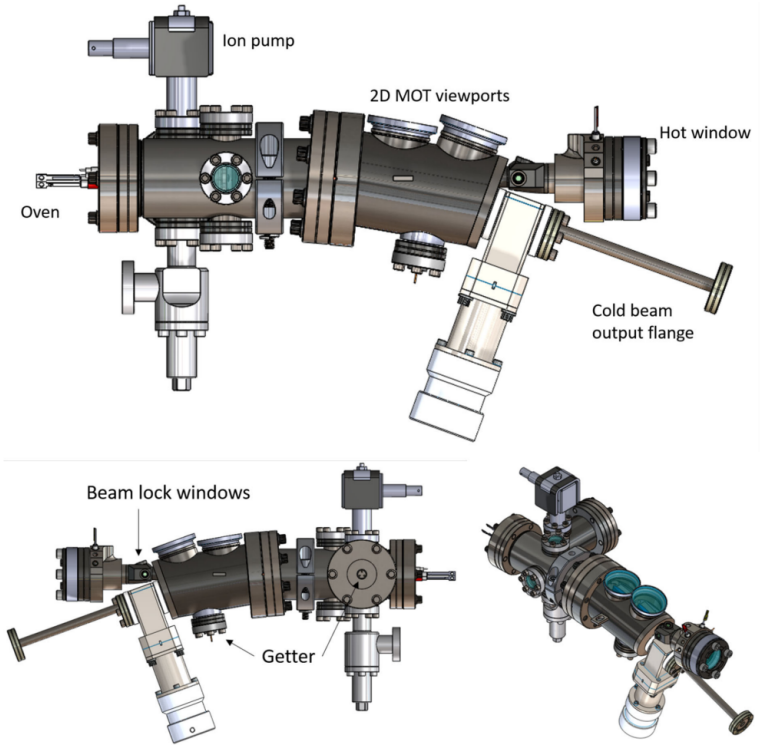

Figure 3.2. All sides of view on the AOsense chamber is presented, highlighting all the built-in components.

The AOsense chamber is a complete cold atomic beam source for Ytterbium precision experiments and atomic devices. It is provided with small chambers with permanent-magnet Zeeman slowers and in-vacuum 2D MOT optics that allow for collimation, slowing and deflection of the atomic beam. As shown in Fig. 3.1, it is designed to store an atomic beam that starts its path from the oven, then it is slowed by a Zeeman slower, collimated and by two 2D MOT beams into the cold beam output flange. It also includes some small windows

(beam lock windows in the drawing) used for spectroscopy. It is provided under vacuum and present all the components needed to keep the pressure below 10^{-9} mbar (ion and getter pumps and a flange to connect a turbo pump in case of need) even while the oven is at working temperature. It provides all the details needed for laser beam alignment on it: power, which needs to be above 35 mW total for the 2D MOT beams and above 50 mW for the Zeeman slower, polarization, that is right-handed circular polarization for all of the beams, waist of the beams, detuning from resonance and oven working temperature (400-420 °C). Since the hot atomic beam is directed to the Zeeman slower, to guarantee its correct functioning and stability over time, its window has to be heated up to 330 °C in order for Ytterbium atoms not to stick on it.

3.1.2 Pumping chamber

The main pumping chamber, supplied by SAES Getters, is shown in Fig. 3.3 together with all its components.

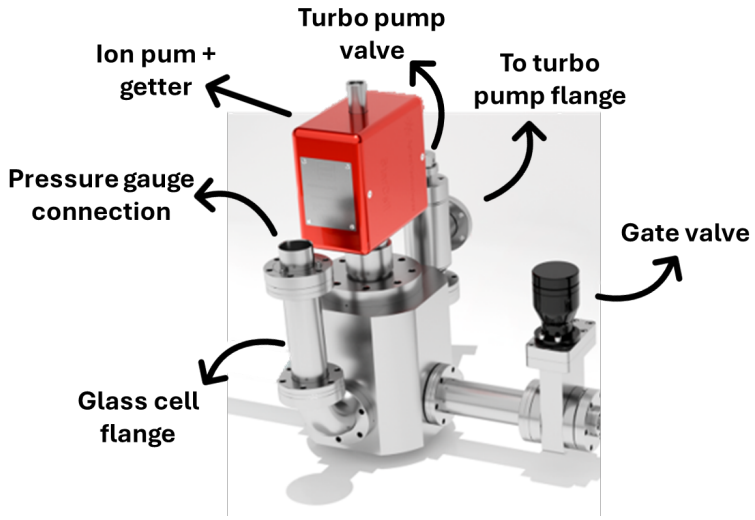

Figure 3.3. The pumping chamber is illustrated with all its components.

It is the main chamber, where all the stages of vacuum pumping and bakeout are carried out. It is provided with two valves that allow the isolation of every component. One is positioned right after the flange that connects AOsense chamber and pumping chamber (gate valve in figure) and, since the AOsense chamber was delivered already under optimal pressure conditions, it was opened only after the first bakeout of the pumping chamber. The other is needed to close the connection to the turbo pump after the first pumping and bakeout stages. It also includes an ion pump and a getter pump, needed in the last stages of vacuum to reach ultra-high vacuum conditions (below 10^{-10} mbar). The functioning principle of these pumps is explained in the following section. The bakeout procedure allows the temperature to reach up to 250 °C in most parts of the chamber. However, there are two locations where particular care must be taken: the gauge connection, which must remain below 150 °C, and, if

the bakeout is performed with the glass cell attached, the area near the flange connecting the pumping chamber to the glass cell, which is also at risk.

3.1.3 Glass cell

The glass cell is fundamental for the experiment, as it will host the atoms trapping stages and the final quantum computing platform in its entirety. It made out of quartz by optical contact. Since all the lasers will need to cross the glass cell, and in particular the 556 nm MOT will have an angle of $\simeq 60°$ with respect to its upper and lower sides, an anti-reflection coating is needed. the coating is present only on the outside surface of the upper and lower sides of the cell With a reflectance which is dependent on the angle and it is shown in Fig. 3.4

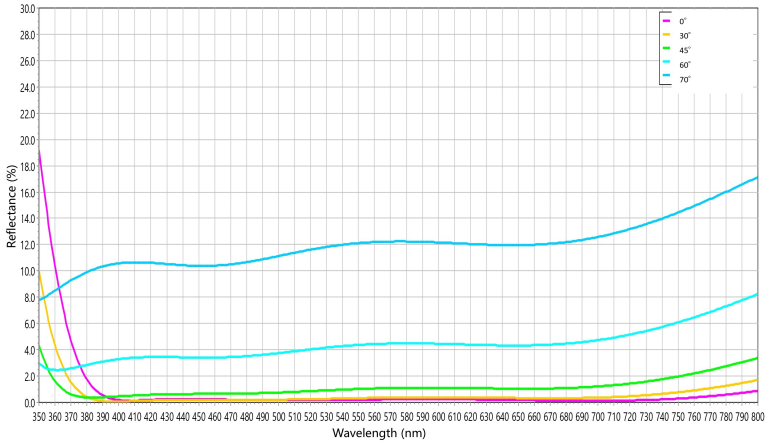

Figure 3.4. Plot of the upper and lower cell faces reflectance as a function of the wavelength. these two sides have an anti-reflection coating for wavelengths between 399 nm and 759 nm.

It is also provided with a rotatable flange that allows for better alignment as shown in Fig. 3.5.

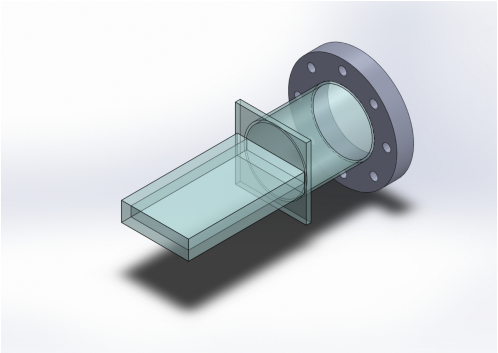

Figure 3.5. Drawing of the glass cell. The visible flange is rotatable and connects it to the pumping chamber.

3.2 Assembly of a ultra-high vacuum system

To build ultra-high vacuum (UHV) systems, few components are required, but the process of mounting them has to be carried out with utmost precision.

The most critical part is the connection between any two parts of the setup. If they are not tightly connected they could cause a leak that prevents the system from reaching the orders of pressure needed for the experiment. To overcome this problem, a particular type of flanges, called CF (ConFlat) flanges, were engineered and have become a standard for UHV systems. This type of flanges, showed in Fig. 3.6 are sealed by a copper gasket, that, deforming under the pressure of the tightening screws, totally fills the space between the two flanges. Each face of the two mating CF flanges has a knife edge, which cuts into the softer metal gasket, providing an extremely leak-tight, metal-to-metal seal. Deformation of the metal gasket fills small defects in the flange, allowing ConFlat flanges to operate down to 10^{-13} Torr (10^{-11} Pa) pressure. The knife edge is recessed in a groove in each flange. In addition to protecting the knife edge, the groove helps holding the gasket in place, for the alignment of the two flanges and also reduces gasket expansion during bake-out.

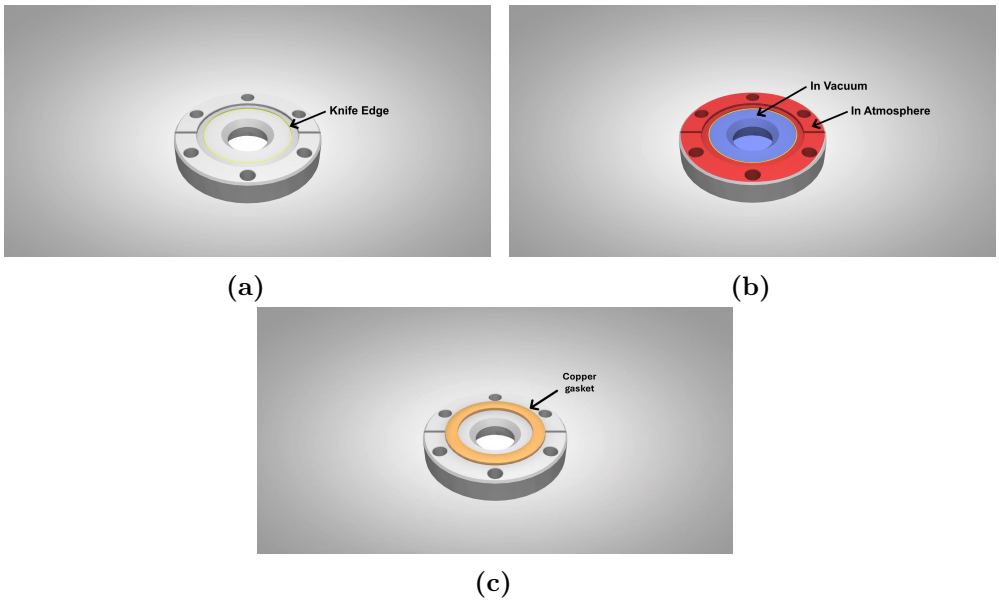

Figure 3.6. Representation of a CF flange. (a) The image shows the structure of the flange and the position of the knife edge. (b) The knife edge divides the part of the flange that is in contact with external atmosphere and the part in contact with vacuum. (c) Position of the gasket on the flange. It places in a groove where the knife edge is engraved.

Two flanges can be connected thanks to six screw holes present in the external parts. To make sure that no leak is created during the screwing, one has to tighten the screws in a way that keeps the pressure on the gasket uniform as shown in Fig. 3.7. In particular, one has to tighten the screws in small steps and in pairs on opposite sides of the flange, making sure that, at each step, the

distance between the two flanges is uniform on the whole surface.

Another fundamental ingredient for ultra-high vacuum are pumps. Three different types of pumps are needed in the case of this thesis: turbo pumps, ion pumps and getter pumps. Briefly, turbo pumps employ multiple stages of rapidly rotating rotor and stator blades to transfer momentum to gas molecules, directing them toward a mechanical backing (fore) pump; they offer high pumping speeds for light gases but require a forepump and careful vibration isolation. Ion pumps operate in ultra-high vacuum by electron-impact ionization of residual gas; the resulting ions are accelerated by a large voltage difference ($\sim$ KV) onto cathode surfaces where they are captured. Getter pumps use reactive metal surfaces (e.g., Zr-based alloys) that chemically absorb and bind active gas species (H_2, O_2, CO, ...), supplying continuous pumping for reactive gases after activation. The activation consists of heating the getter material in vacuum up to few hundreds of °C. This heat treatment removes surface oxides exposing the reactive metal.

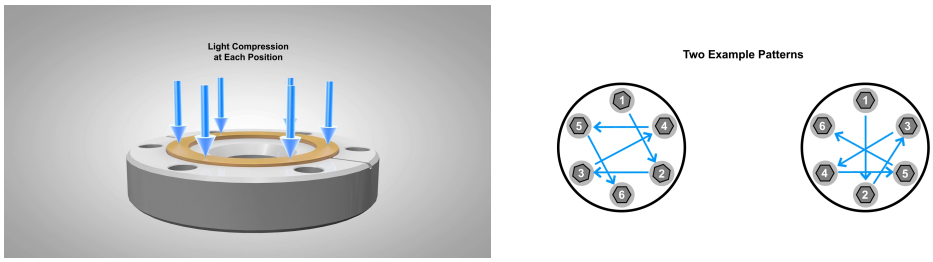

(a) **(b)**

Figure 3.7. (a) Uniform pressure has to be exerted on the gasket in order to prevent vacuum leaks. (b) Two example screwing patterns where screws are gradually tightened in pairs on opposite sides, continuously checking the space between the two flanges with a feeler gauge.

3.3 Pumping and bakeout

Since at the beginning of the assembly of the vacuum system, the glass cell had not been delivered yet, the pumping and bakeout procedure described below were carried out two times: one with just the AO-sense and pumping chambers, where the connection to the glass cell was blocked by a blind flange, and one with the AOsense chamber, pumping chamber and glass cell. The process is as follows:

1. Attach the turbo pump to the pumping chamber. Operating it allows us to reach a pressure of $\sim 10^{-7}$ mbar, even $\sim 10^{-8}$ mbar in the best cases. In this thesis, it reached $2.1 \cdot 10^{-7}$ mbar after 14 hours of operation.

2. *Bakeout process*: it is a process where the whole vacuum system is heated up to $\sim$ 200/250°C , needed to drive out volatile compounds, water vapor, and other adsorbed contaminants from the surfaces and interiors of the

vacuum system. During the process the pumping chamber removes all the compounds that are outgassed. In the case of this thesis the bakeout was carried out two times (one time without the cell and another with the cell); each time the temperature was measured in several points during the whole process. The temperature measurement is necessary because during the whole process we have to be sure that it is uniform and the increase is not too fast; furthermore, the temperature must not exceed the limits given in the previous section. To ensure temperature uniformity, the heating tape were placed as uniform as possible and then, the whole system was covered by multiple layers of aluminum foil. The process is also monitored measuring the abundance of different chemical compounds via RGA (residual gas analyzer). The RGA working principle is very similar to a mass spectrometer. It operates by ionizing gas molecules through electron impact and then separating the resulting ions according to their mass-to-charge ratio (m/q). The ions are detected by a collector, and their signal strength provides information about the partial pressures of the various species in the chamber. In Fig. 3.8 and 3.9 the RGA spectra at the beginning and at the end of both the bakeout processes, together with the log of temperatures vs time, are shown

3. After closing again the valve between turbo pump and pumping chamber and disconnecting the turbo pump, the ion pump is switched on, allowing the system to reach pressure of $\sim 10^{-10}$ mbar, measured with the gauge sensor connected to the pumping chamber.

4. Activation of the getter pump. For the activation the temperature has to reach 600°C. The reading reached on the ion pump controller reached $9.2 \cdot 10^{-13}$ mbar.

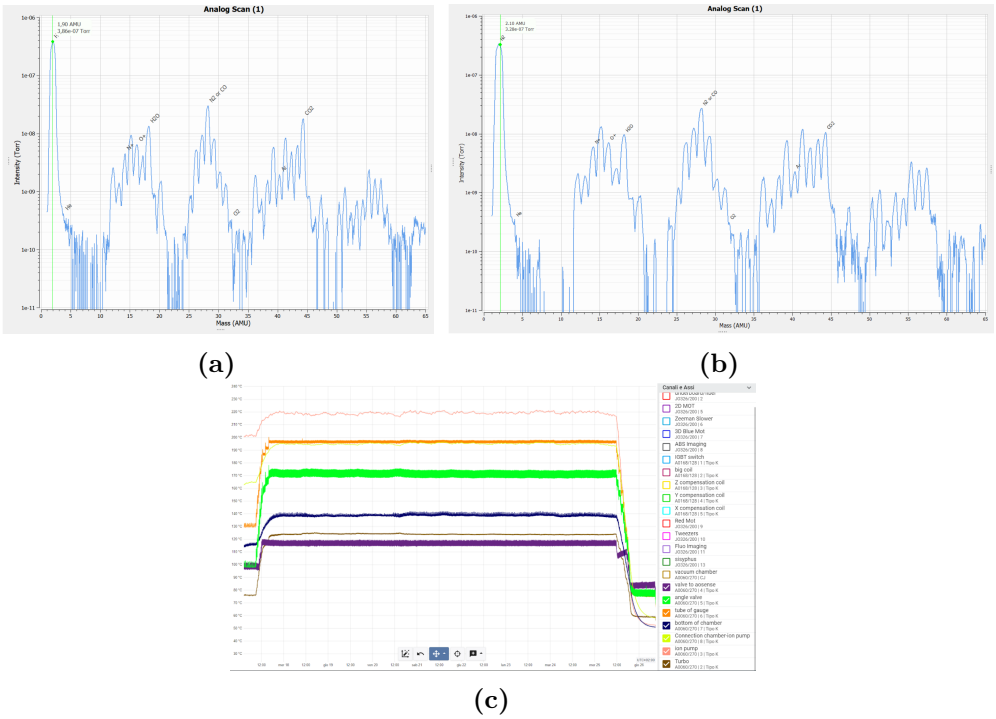

Figure 3.8. RGA spectra at the beginning of the first bakeout on 19/06/2025 (a) and at the end on 26/06/2025 (b). (c) Temperature vs time during the first bakeout.

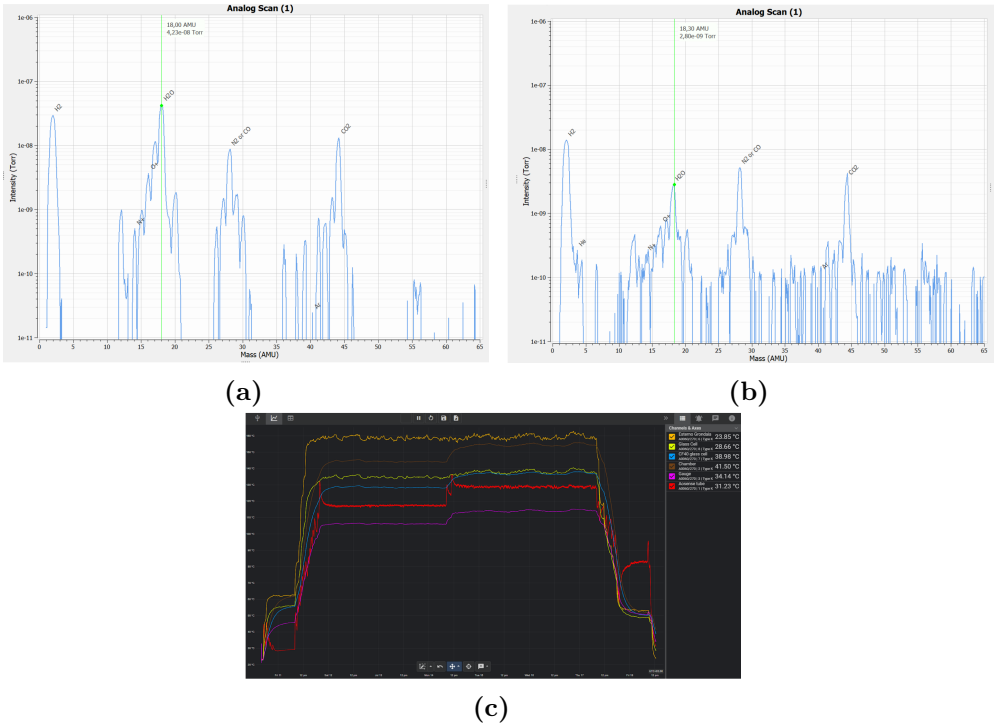

Figure 3.9. RGA spectra at the beginning of the second bakeout on 16/07/2025 (a) and at the end on 18/07/2025 (b). (c) Temperature vs time during the second bakeout.

Chapter 4

Laser system

This chapter will focus on the most consistent part of the thesis work, the laser system. In particular, during this thesis, both the setup for the blue 399 nm laser and part of that for the green 556 nm laser have been built. The laser setups are distributed over two separate optical tables: one hosting exclusively the lasers and laser-related instruments, and another dedicated to the experimental apparatus. From this point onwards, they will be referred to as the laser table and the experiment table, respectively.

On the laser table, both lasers beams are split in several beam paths in order to address all the needed applications. They are then frequency shifted by means of acusto-optic modulators (AOMs) at different detunings and coupled into polarization-maintaining optical fibers that drive the beams on the experiment table.

Here, they are aligned onto the experiment according to their specific function. In the following sections, a detailed analysis of the entire laser system is presented, with particular attention to the alignment procedure, the function of its individual components, and the techniques employed for laser frequency stabilization.

4.1 Blue laser

The 399 nm laser is a commercial frequency-doubled extended-cavity diode laser. The laser is a Toptica laser; provided with a DL pro seed, a TA pro amplifier and the DLC pro digital controller. It is composed of a seed emitting at 798 nm, which is first amplified by a semiconductor tapered amplifier and then frequency doubled in a bow-tie duplication cavity. At full operating regime, the output power reaches ~ 1 W. An overall representation of the optical system built to manipulate the 399 nm light is shown in Fig. 4.1 and Fig. 4.2.

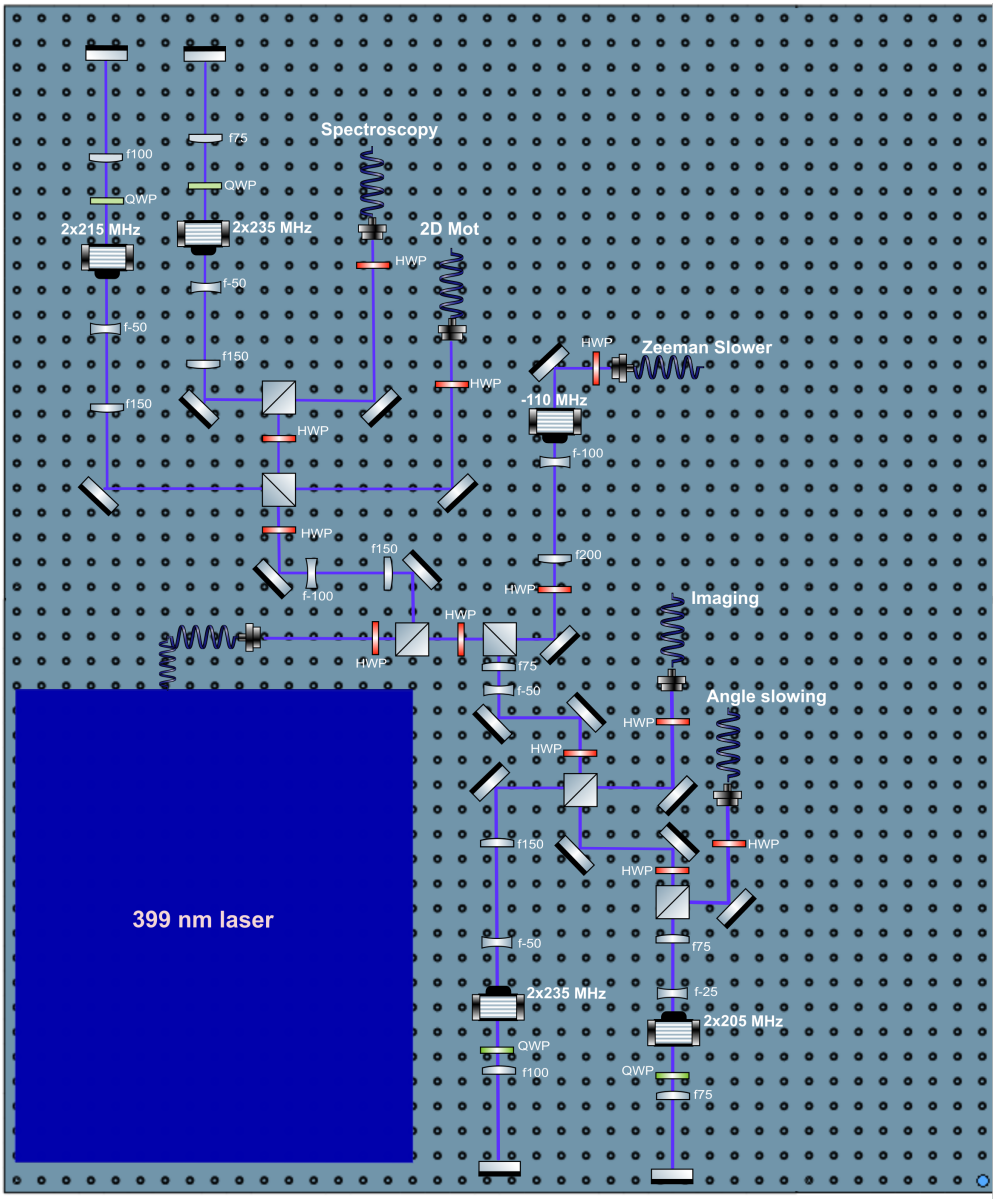

Figure 4.1. Optical setup for the 399 nm light on the laser table.

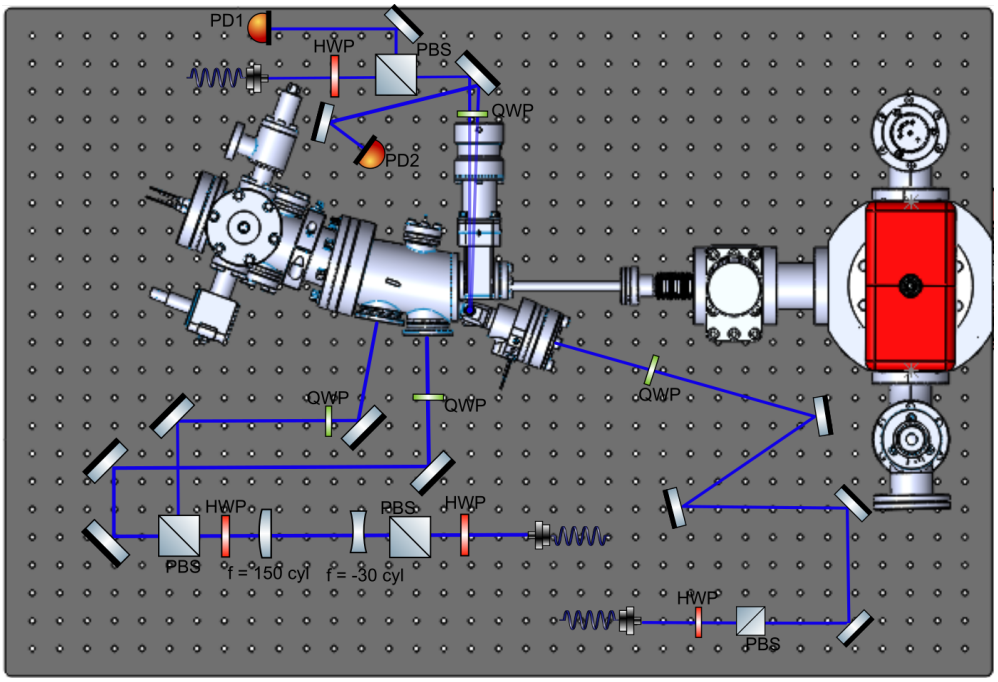

Figure 4.2. Optical setup for the 399 nm light on the experiment table (2D MOT, Zeeman slower and spectroscopy only).

On the laser table, the 399 nm beam is divided into five separate beams using a combination of half-waveplates (HWP) and polarizing beam splitters (PBS). Each of these beams serves a specific purpose and is assigned a different detuning from the carrier accordingly. The detuning of each beam in presented in the scheme in Fig. 4.3 and it is induced using AOMs.

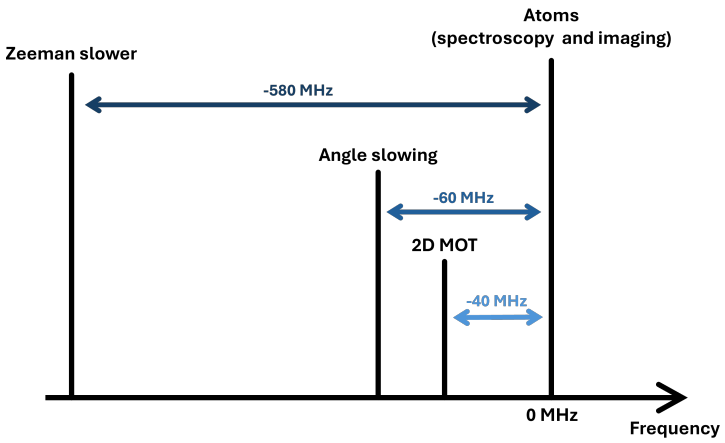

Figure 4.3. Detuning of the blue laser beams considering the atomic resonance as reference frequency (spectroscopy beam).

In order to stabilize the laser emission frequency, we use the atoms as a frequency reference by performing spectroscopy on the $^1S_0 \rightarrow {}^3P_1$ transition

(see sec. 4.1.1), which is implemented by using a beam perpendicular to the atomic beam; hence, at first order there is no Doppler shift and, to be resonant, the light has to match the frequency of the atomic transition. This is why it is used as a reference. For the imaging beam, the same reasoning stands, but in the case it is done on hot (moving) atoms by a not perpendicular beam, the detuning has to be changed accounting for Doppler effect. The detuning of 2D MOT and Zeeman slower were chosen based on the instructions from the AOense team that tested the atomic source, while the angle slowing is calculated accounting for the angle of the beams and the Doppler shift of the transition.

All optical fibers used to transfer the beams from the laser table to the experiment table are polarization-maintaining. To ensure stable polarization at the fiber output, a half-waveplate is placed before each of the fiber input collimators, allowing proper polarization alignment into the fibers.

In Fig. 4.2 the AOsense breadboard is shown. Here the spectroscopy beam, Zeeman slower and 2D MOT are aligned. Imaging and angle slowing beams are not visible because they are aligned on the glass cell.

4.1.1 Spectroscopy

The spectroscopy optical setup is shown in Fig. 4.4.

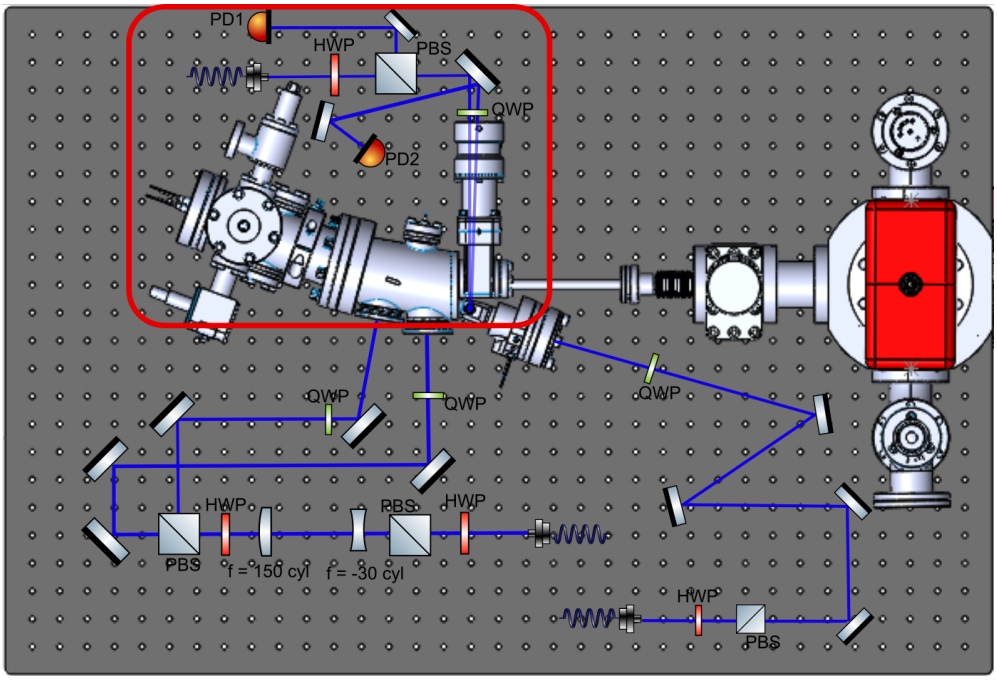

Figure 4.4. Spectroscopy setup circled in red.

Here, the beam is sent through a small window near the end of the atoms path and, after interacting with the atoms and exiting from a second window

(not visible in figure), is then backreflected by a mirror. In Figure 4.4 two beams coming back from the entrance window are represented: one going to the photodiode called PD1 through a polarizing beam splitter (PBS), and another going to PD2. The beam detected by PD1 is the beam after backreflection, which has interacted (twice) with the atoms and whose absorption produces the spectroscopy signal (an example where the $^1S_0 \rightarrow {}^1P_1$ transition is observed for every isotope is shown in Fig. 4.5). The second one, detected by PD2, is the beam produced by the reflection of the incident beam at the entrance window and is visibly separated form the other one because the window is tilted. The signal from PD2 is given as input to the the the control system, which is programmed to generate a signal that opposes to the fluctuations in power that are measured. The control system output is then fed to the spectroscopy AOM to do power stabilization, therefore improving the signal to noise ratio in the spectroscopy. The difference in the signal with and without intensity stabilization is shown in Fig4.7. Note that the spectroscopy is done via absorption signal, meaning that, to optimize the signal in order not to induce power broadenin of the transition, the power has to stay below the saturation intensity of the transition given by:

$$I_{sat} = \frac{\pi hc}{3\lambda^3 \tau} \tag{4.1}$$

Which for the $^1S_0 \rightarrow {}^1P_1$ transition is 59.97 $\frac{\text{mW}}{\text{cm}^2}$. In the case of this thesis the best signal is obtained with $P \sim 5$ mW and a beam waist of few millimeters, meaning $I \sim 10^{-2}$ $\frac{\text{mW}}{\text{cm}^2}$, well below I_{sat}.

4.1.2 Frequency lock

The spectroscopy signal is used as a frequency reference for all of the other beams, because its frequency is exactly that of the atomic transition resonance. Hence, laser locking is performed on the spectroscopy signal.

In particular, depending on the isotope of interest (^{171}Yb in this case), the laser is locked to one of the two ^{171}Yb peaks shown in Fig. 4.5 (the two ^{171}Yb peaks refer to the two hyperfine components of the $^1S_0 \rightarrow {}^1P_1$ transition of this isotope). The lock was achieved using the internal functionalities of the laser controller, which includes a built-in PID controller and the capability to modulate the laser output. This allows the system to avoid external modulation through AOMs. The modulation is applied to the piezoelectric actuator that controls the extended cavity of the diode laser.

The error signal shown in Fig. 4.6 is obtained through modulation and demodulation of the laser at the same frequency. In particular we are in the low frequency modulation case of PDH technique (modulation frequency 1 KHz $\ll \Gamma \simeq 29$ MHz), explained in sec. 1.4.3, where instead of a reference cavity, the reference is given by the spectroscopy peak.

The lock parameters are chosen following the Ziegler-Nichols method explained in sec. 1.3.1 and further optimized manually:

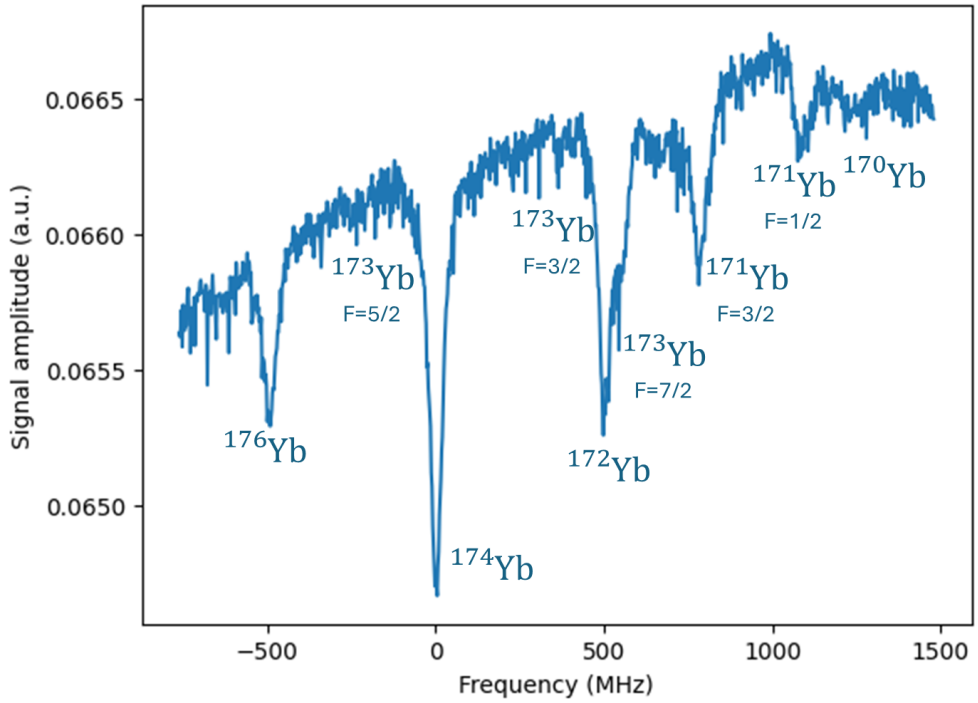

Figure 4.5. Spectroscopy signal with an oven temperature of $\simeq 420°$. The frequency of the laser is scanned over a range high enough to observe the $^1S_0 \rightarrow {}^1P_1$ transition for all of the Yb isotopes.

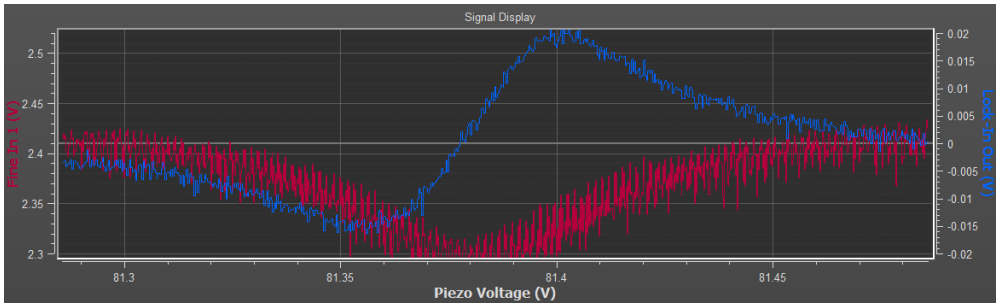

Figure 4.6. Spectroscopy error signal obtained via ~ 1 kHz modulation frequency and 0.05 mA pp modulation amplitude. Two signals are visible: in red the spectroscopy signal corresponding to the ^{174}Yb peak and in blue the corresponding error signal generated by demodulation of the spectroscopy signal at the modulation frequency. Since ^{174}Yb shows the biggest spectroscopy peak, it is used here as an example to show a clear signal despite actually locking on ^{171}Yb.

P(V/V)	I(V/V/ms)	D(V/(V·ms)
0.01	0.01	0

Intensity stabilization of the laser is crucial for the locking on ^{171}Yb because of its small signal amplitude with respect to other isotopes. The difference in the error signal between intensity-stabilized and not intensity stabilized is

shown in Fig. 4.7

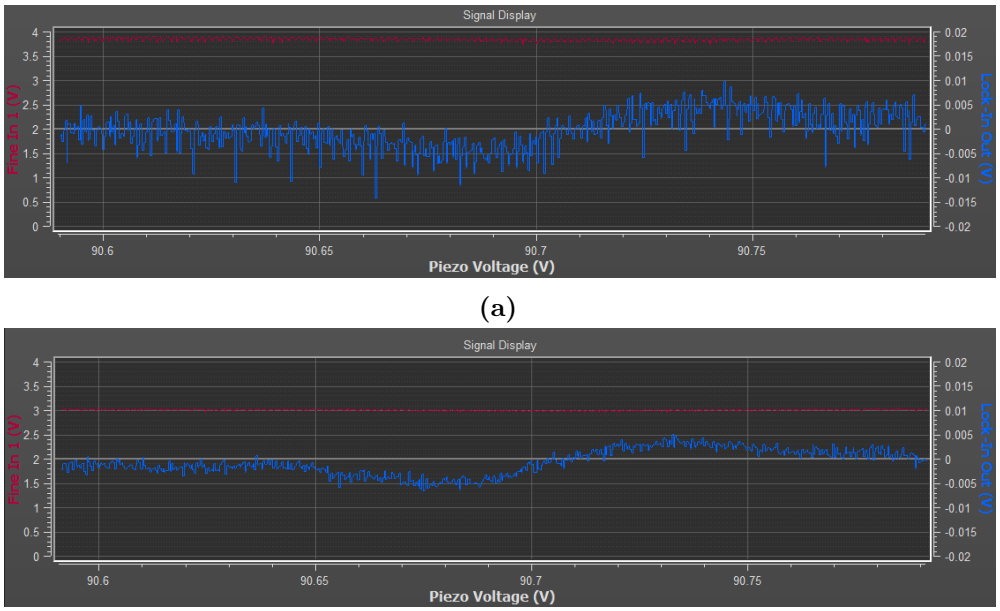

(a)

(b)

Figure 4.7. ^{171}Yb spectroscopy error signal without (a) and with (b) laser intensity stabilization.

The intensity-stabilized signal is smoother and exhibits a clear slope, in contrast to the signal without intensity stabilization, where the noise almost completely covers the slope, preventing the PID from applying effective corrections. The lock is implemented following the same procedure as the one implemented on ^{174}Yb (same modulation amplitude and frequency) and the same parameters stand:

P(V/V)	I(V/V/ms)	D(V/(V·ms)
0.01	0.01	0

4.1.3 2D MOT

The 2D MOTs optical setup is shown in Fig. 4.8. Two cascaded 2D MOTs are needed to collimate the atomic beam and deflect it into the glass cell and they are realized starting from the same 399 nm laser beam, split in two by a PBS. The magnetic field gradient is created by permanent magnets installed in the atomic source.

All the specifications needed for the optimization of the 2D MOTs are given by the manufacturer. In particular, the beam has to be elliptical with an approximate dimension of 25×5 mm, the total power has to be above 25 mW with a 2:1 power ratio between the first and the second trap and the polarization

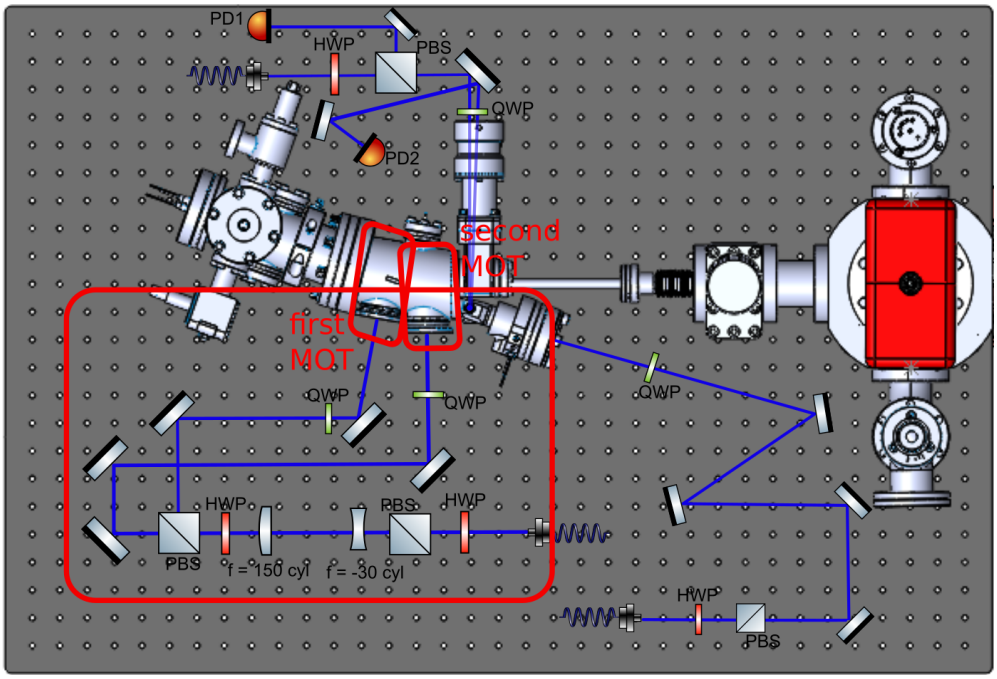

Figure 4.8. 2D MOT setup circled in red.

has to be circular right-handed for both traps.

To guarantee all these characteristics are satisfied, the collimator ate the fiber output is chosen so that the beam exiting from the fiber has a 8 mm diameter. Then it is reshaped by two cylindrical lenses and divided into two beams by a PBS. To regulate the power ratio between the beam a half-waveplate is placed before the PBS. Finally, to ensure proper polarization of the beams, a quarter-waveplate is placed before each of the windows.

The manufacturer also recommends a detuning of -40 MHz from resonance for the MOT beams, which is reasonable given that optimal detuning in a MOT is $\sim -\Gamma$. The detuning is given by a double-passage configuration AOM on the laser table as described in the previous section.

4.1.4 Zeeman slower

The Zeeman slower optical setup is shown in Fig. 4.9.

As in the case of the 2D MOTs, the optimal specifications are given by the manufacturer.

The Zeeman slower is implemented through a magnetic field induced by a permanent magnet installed in the AOsense chamber and a counterpropagating laser beam along the direction of the atomic beam. The Zeeman slower is -580 MHz shifted from spectroscopy frequency, the suggested beam diameter is between 6 mm and 8 mm and it has to slightly focus into the oven. The polariza-

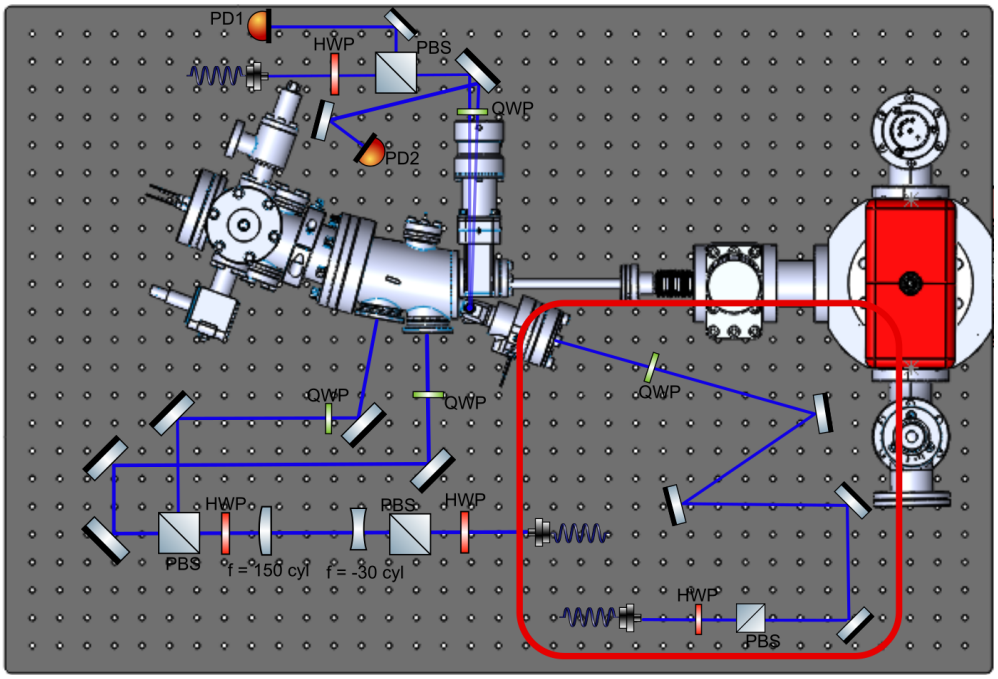

Figure 4.9. Zeeman slower setup circled in red.

tion has to be circular right-handed and the total power has to be above 50 mW.

As a result, the collimator at the fiber output is chosen such that the beam has a diameter of 8 mm at the fiber output, then a half-waveplate and a PBS are placed to adjust the beam power. Finally a quarter-waveplate is placed before the window to adjust the polarization of the beam.

The combined effect of Zeeman slower and 2D MOTs, is illustrated in Fig. 4.10, together with the following slowing and trapping stages of the 399 nm angle slowing and the 556 nm 3D MOT.

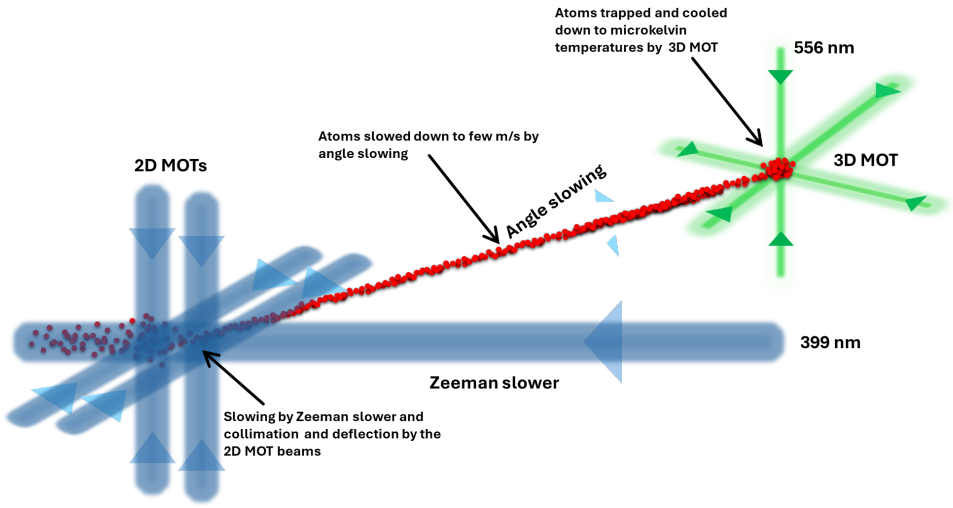

Figure 4.10. Illustration of the atomic beam path. The atoms are first slowed, collimated and deflected by the combined effect of Zeeman slower and 2D MOTs. After the deflection they are slowed again by two angle slowing beams down to the capture velocity of the subsequent green 556 nm MOT.

4.2 Green laser

The green laser is a high power fiber laser. It is the ALS VIS system by Toptica Azurlight. It is formed by an seed at 1112 nm provided by NKT photonics, model Koheras Basik Y10, followed by two amplification stages and a frequency doubling by second harmonic generation stage. Its maximum emission power is 1 W and the linewidth is < 10 KHz.

The green laser optical setup is divided into three main parts: actual optical setup on laser table and experiment table and the ULE setup, where the non frequency doubled laser (infrared seed) is used for frequency stabilization. At the moment of the writing of this thesis, the green laser setup on the laser table has not been built yet, but the project is shown in Fig. 4.11.

As shown in figure, the main beam is split into six paths, depending on the application. In fact the green laser is the most important one for the experiment because of its several uses. It is used in the first stages of atom cooling to create a 3D MOT that traps and cools atoms down to microkelvin temperatures. Once the atoms are trapped in optical tweezers, it is used to optically pump the atoms for the intialization of the qubits (all qubits are pumped to the ${}^1S_0, |m = -\frac{1}{2}\rangle$ state, which is the $|0\rangle$ qubit state) and to drive single qubit gates via Raman transitions. Finally it is used also for imaging.

All of these applications, based on the (quasi) resonant driving of the ${}^1\mathrm{S}_0 \rightarrow {}^3\mathrm{P}_1$ transition, imply that the laser frequency stability should satisfy $\Delta\nu_{\mathrm{laser}} \ll \Gamma$, i.e. the frequncy fluctuations need to be much smaller than the transition linewidth Γ. For the 556 nm transition $\Gamma \simeq 2\pi \cdot 182$ kHz, meaning the reference signal for the lock must be significantly more stable than in the case of

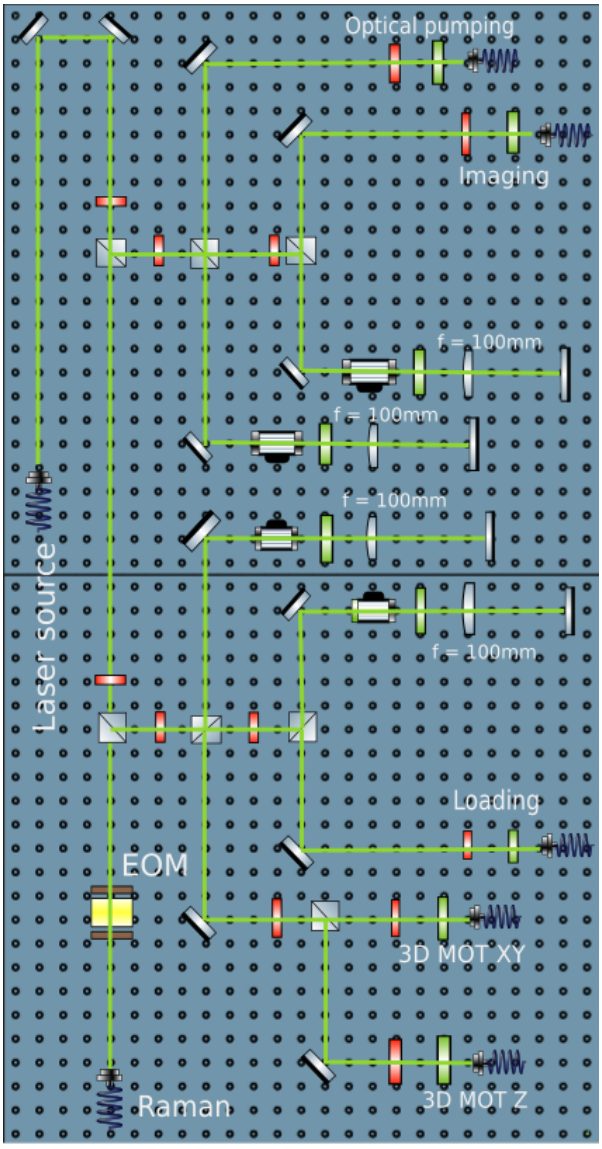

Figure 4.11. Green laser setup on laser table.

the blue transition. This time it is difficult to lock directly on the spectroscopy signal, and it would require a first stage of stabilization on a reference cavity, because the transition is $\sim 10^2$ times weaker than the $^1S_0 \rightarrow {}^1P_1$ transition. Hence, in the following sections, two alternative locking methods are proposed: a lock on a ULE (ultra low expansion) cavity and offset lock, where the error signal is given by the beatnote between a reference laser (already locked in some way on the atomic transition of interest) and the laser that has to be locked.

4.2.1 ULE cavity

An ULE cavity is an optical cavity whose body is made out of ultra-low expansion glass, which has a very low coefficient of thermal expansion and contains as

components silica and less than 10% titanium dioxide. Since the free spectral range depends on the length of the cavity as FSR $= \frac{c}{2l}$, variations in the cavity length l due to thermal expansion of the material result in a corresponding shift of the resonance frequencies. For this reason, ULE glass is employed, as its extremely low coefficient of thermal expansion (zero at first order around a working temperature T_0, typically close to room temperature) minimizes such shifts and can ensure long-term frequency stability.

The ULE cavity employed in this experiment is shown in Fig. 4.12. It is the ORC-Cubic cavity by provided by Menlo Systems. It consists of a 5 cm long cubic spacer built out of ULE glass and two high finesse mirrors, also made out of ULE glass.

Figure 4.12. ULE cavity. Two high-reflectivity mirrors in Fabry-Perot configuration are optically contacted to a monolithic cubic cavity.

The light incoupling mirror is a plano-concave mirror with a radius of curvature of 1 m. The outcoupling mirror is a plano-planar mirror. It is an optically contacted cavity, meaning that the mirrors are directly connected to the ULE glass spacer using a process called optical contacting, where two closely conformal surfaces are joined, being held purely by intermolecular forces. Nominally, the cavity has a 3 GHz free spectral range and 300000 fo finesse @1064 nm, resulting in a linewidth of $\sim$ 10 KHz. The mirros have multiple wavelength coating for 556 nm, 600-620 nm and 1112 nm.

The cavity is mounted in a vacuum chamber made out of aluminum and ConFlat flange components with small leaking rates. It is provided already under vacuum and with an ion getter pump that ensures the pressure to always stay below 10^{-7} mbar. The vacuum chamber is also equipped with two viewports as shown in Fig. 4.13. The cavity is mounted inside the chamber

with a small angle relative to the viewports in order to avoid etaloning effects. The distance between the mirrors and the viewports on both sides is 5.7 cm.

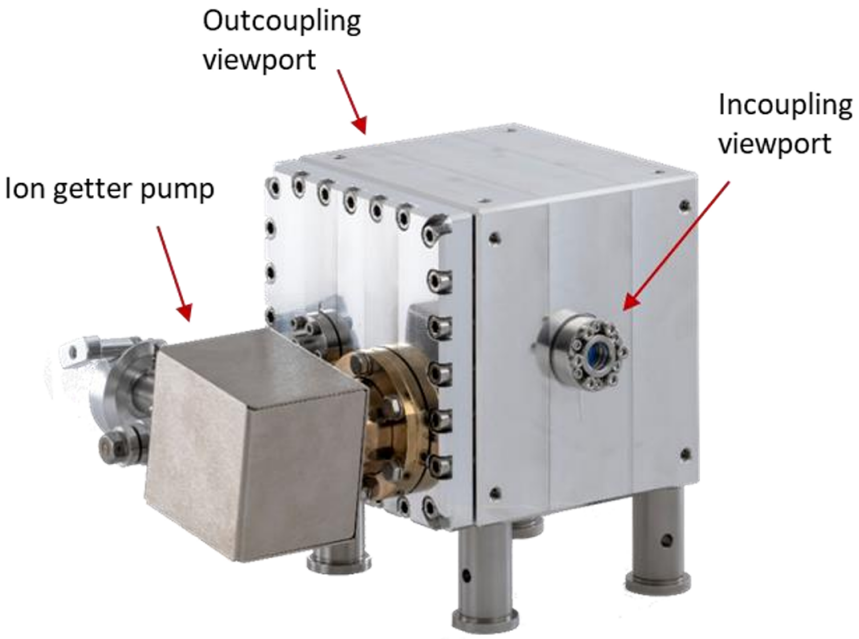

Figure 4.13. Vacuum chamber that hosts the ULE cavity, provided with two viewports and an ion getter pump.

The cavity is also thermally stabilized via an external temperature controller.

The optical setup implemented to align the 1112 nm beam into the cavity is shown in Fig. 4.14. It is mounted on a breadboard vertically attached to the ULE cavity input facade; the black circle drawn in figure is the hole corresponding to the cavity viewport and, there, a 45° mirror is placed to deflect the beam into the hole. The optics were chosen on the basis of a cavity mode matching calculation. In particular, the collimator at the fiber output has a focal length of 4.6 mm, that, combined with the numerical aperture of the optical fiber used, gives an initial beam waist of 0.6 mm. The collimated beam crosses a half-waveplate and a PBS in combination, to adjust the incoming power in the cavity, that has to be strictly below 100 μW in order not to damage the cavity. The immediately subsequent lens with 500 mm focal length is positioned at a distance $d \simeq 300$ mm from the first viewport, so that the beam has a curvature radius of -1000 mm (the same as the mirror curvature) at the position of the first cavity mirror and is focused at the position of the second mirror, which represent the boundary conditions for the mode matching. The quarter-waveplate is meant to rotate by 90° the beam polarization of the reflected light that passes twice through it, so the PBS sends all the reflection to the fast photodiode.

Beam alignment on the ULE cavity is very delicate and requires different steps. First a Thorlabs camera was placed right after the output viewport to observe the shape of the exiting beam while a frequency scan of the laser was

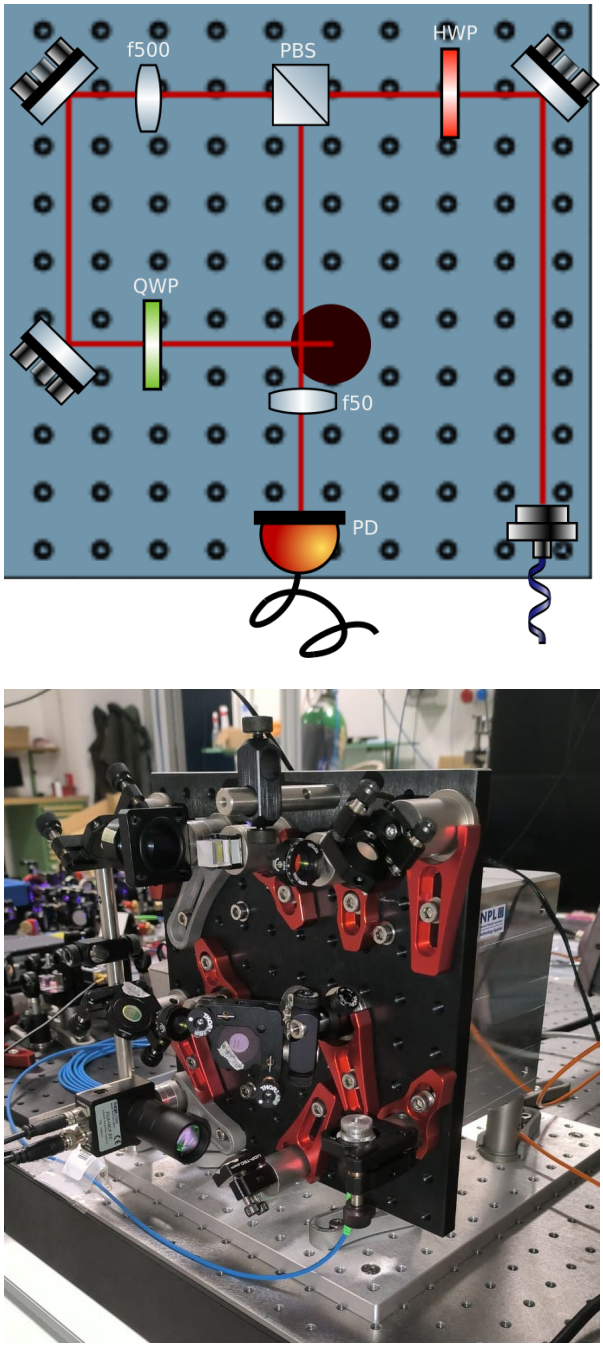

Figure 4.14. Optical setup designed to align the beam into the cavity, showed together with a picture of the actual realization in the laboratory.

performed. The reason is that when the beam shape properly matches the fundamental transverse mode of the cavity, the cavity transmission mode should be a perfect TEM00, where all the transmitted power is condensed; while with bad mode matching, the cavity transmission varies along one scan and presents different modes with very low power. Initially, the laser has to be scanned over the whole free spectral range of the cavity in order to be sure of observing a

transmission peak. In the case of this thesis the scan is done with the internal ramp option of the laser. Selecting a high gain in the camera a signal was detected and optimized through fine tuning on the alignment. The scan was then narrowed around the peak in steps, tuning the alignment in each step until a good TEM00 mode is observed, with suppression of the other modes. In Fig. 4.15 two beam shapes recorded during alignment are shown: a TEM10 and a TEM00.

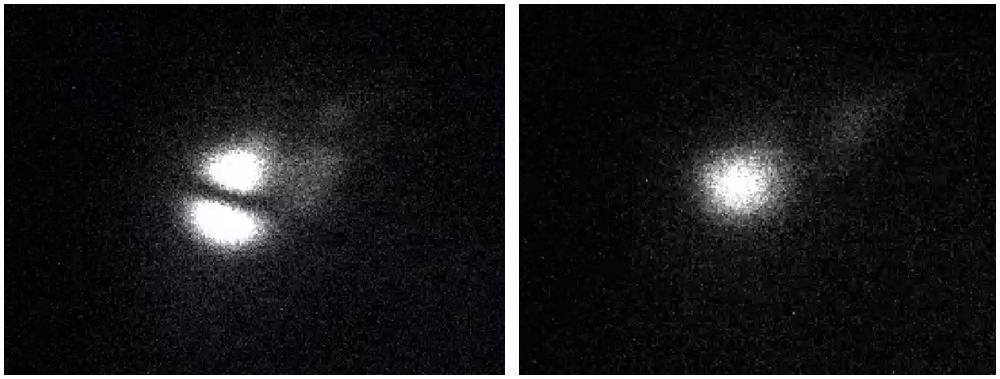

(a) **(b)**

Figure 4.15. Example of two Hermite-Gaussian modes observed during cavity alignment. (a) TEM10 and (b) TEM00.

Once the TEM00 is observed, the subsequent step consists in optimizing the reflection signal from the photodiode. The signal consists of a reflection dip (corresponding to the resonance frequency of the cavity) in a flat signal offset (power of the laser). The best signal obtained and used to lock is shown in Fig. 4.16, showing the amplitude of the reflection dip being $\simeq 20\%$ of the base level, which is enough to generate an error signal, as illustrated in the next section.

4.2.2 Lock on ULE cavity

Unfortunately, during the attempts to lock the laser in july 2025, some issues were encountered with the laser. Any external input for the frequency scan stopped functioning, most likely due to an electronic problem with the seed laser. Since the feedback loop necessarily needs an external input on the laser to be closed, a proper lock could not be performed. At the moment of writing this thesis, the laser is back to the manufacturer for repair. In this section the error signal generation is described.

The error signal is generated via the PDH technique already described in sec. 1.4. The generation and manipulation of the electronic signals is implemented with a Red Pitaya: it is a high-speed signal acquisition and processing board, which allows the modulatation of the signal and its demodulation at an arbitrary frequency order, meaning it can be used also for higher order derivative signal

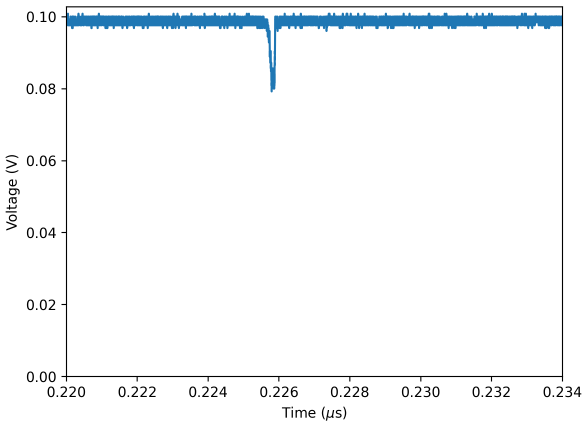

Figure 4.16. Cavity reflection signal. The dip appears when the scanning frequency of the laser crosses the resonance frequency of the cavity. The x axis is in time, but it is directly connected connected to the frequency because the laser scans with a frequency ramp that is linear as a function of time. Estimating a conversion factor between time and frequency is not easy because of how the internal frequency ramp of the laser works, given that it does not provide the frequency corresponding to a certain amplitude of the scan.

generation. It is also provided with a low-pass filter, needed to discard the high frequency part of the signal after the mixer. The optical setup used for the modulation of the signal is shown in Fig. 4.17.

The frequency modulation on the beam is realized sending the modulation signal of the Red Pitaya to the AOM, which is in double-pass configuration. The PDH technique is implemented in high frequency regime (modulation frequency much greater than the cavity peak linewidth of ~ 10 KHz) with a modulation frequency of ~ 8 MHz, in order to have a higher servo bandwidth. The generated signal is shown in Fig. 4.18

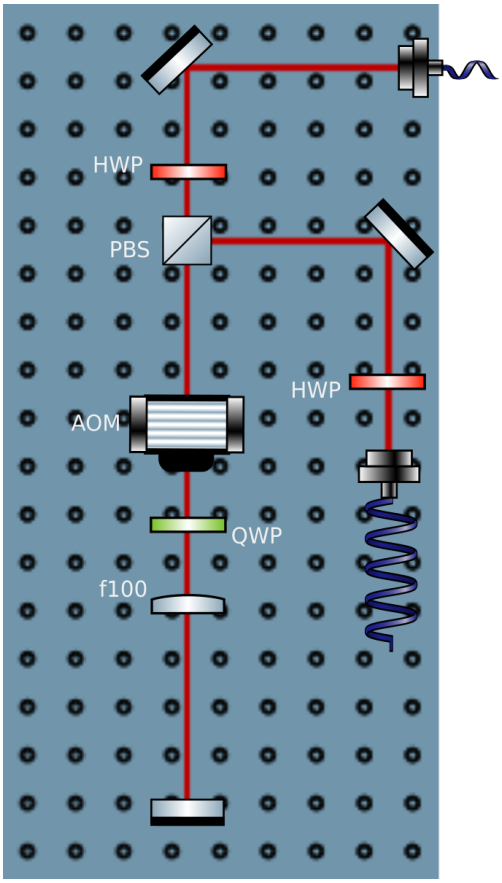

Figure 4.17. Optical setup for frequency modulation of the 1112 nm beam. The modulation is realized via AOM in double pass configuration.

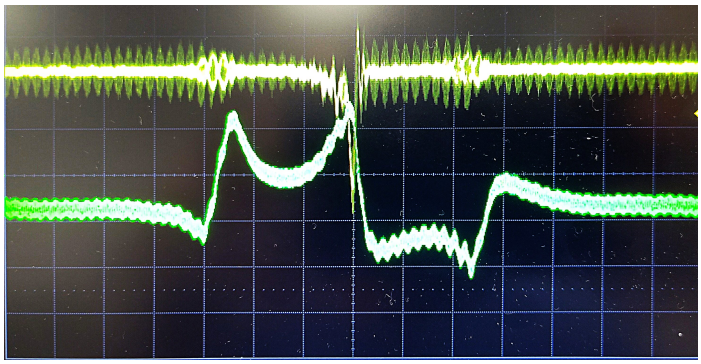

Figure 4.18. Picture of oscilloscope traces showing the generation of the error signal for ULE cavity lock by the PDH technique. The horizontal axis displays the time dependence, which is directly connected to the frequency since the frequency is linearly ramped with respect to the time. Both the modulated reflection signal (yellow) and the error signal (green) are visible. Unfortunately we don't dispose of a better image or plot of the signal, because it was not taken before sending the laser back to the manufacturer.

4.2.3 Offset lock

The second technique implemented for the green laser lock is the offset lock[27]. The setup used for the lock is shown in Fig. 4.19.

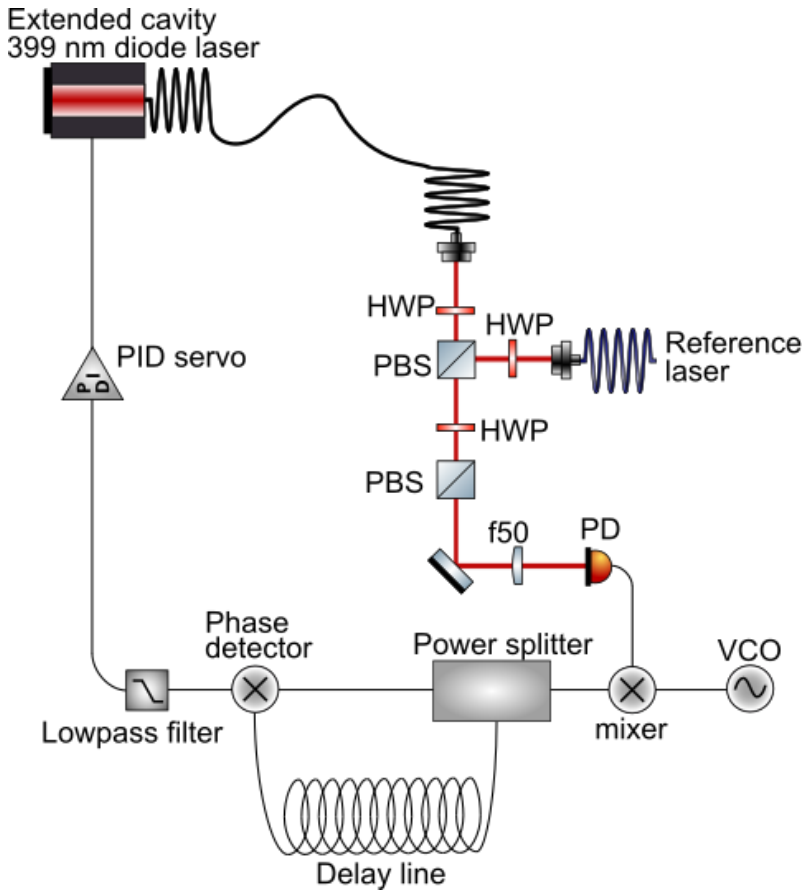

Figure 4.19. Optical and electronics setup for testing the offset lock on the 399 nm laser.

Because the green laser was not functioning, the offset lock was performed on the blue laser, despite it not being the laser of interest. This was done in order to validate the technique and acquire the necessary experience for its future implementation on the green laser.

An offset lock consists in stabilizing the laser using as reference another laser already locked on the transition of interest. To do it, an error signal is generated starting from the beatnote of the two lasers. In the case of this thesis, the reference laser used is a frequency-stabilized 399 nm laser operating in a different laboratory of the department, and its light is delivered to our laboratory via optical fiber.

The optical setup is illustrated in the upper part of Fig. 4.19. Both the lasers pass through a half-waveplate that allows us to adjust the power after the first PBS. It is important to note that, in order to have a good beatnote

signal, the power of the two lasers should be of the same order of magnitude (in the case of this thesis it was around 200 μW). After the PBS, since one beam was transmitted and the other reflected, the relative linear polarization of the two is rotated by 90° and no interference would be observed. Then, another half-waveplate is placed. It is used to rotate the beams polarization by 45°, so that both are partially transmitted by the following PBS. Finally the beams are focused on a photodetector. At this point, before sending the signal in the electronic circuit, it is always checked on a spectrum analyzer that the frequency difference between the two beams is below the bandwidth of the photodiode.

The electronic part, shown in the lower part of Fig. 4.19, is formed by a local oscillator (VCO), that generates a signal at frequency ν_{vco} and amplitude chosen similar to that of the photodiode signal. The two signals are then fed to a mixer that outputs a signal with frequencies given by sum and difference of the two input frequencies: $\nu^+ = \Delta\nu + \nu_{vco}$ and $\nu^- = |\Delta\nu - \nu_{vco}|$, where $\Delta\nu$ is the beatnote frequency. The part of the signal used for the generation of the error signal is the difference signal ν^-, while the sum signal will be discarded later by a low pass filter. Now, the signal is split in a direct and a delayed line by a power splitter and then rejoined in a phase detector. The high frequency part is then cut by a low-pass filter and the final output voltage varies as $\cos(\Phi)$ where Φ is the shift produced by the delay line and is given by:

$$\Phi = 2\pi(\Delta\nu - \nu_{vco})\tau \tag{4.2}$$

where τ is the delay introduced. Physically, the delay line is just a coaxial cable, where the length of the cable determines the delay.

The local oscillator frequency was chosen to be $\nu_{vco} = 50$ MHz. To obtain an optimal signal, different combinations of low pass filter and cable length were tested. In particular all the combinations of low pass filter cutoff frequency $\nu_{cutoff} = 10$ MHz, 50 MHz, 1.9 MHz, cable length $l = 12$ m, 4 m were tested. Two examples of error signal are shown in Fig. 4.20.

The signal chosen for the lock is the one obtained for $\nu_{cutoff} = 1.9\ MHz$ and $l = 4\ m$ (Fig. 4.20b). The lock setpoint is the zero-crossing frequency and it can be shifted by adjusting the local oscillator frequency.

The lock was done in two ways: using the internal PID of the 399 nm laser controller and using an external PID designed by the LENS electronic workshop. In the internal PID case, the The modulation is applied to the piezoelectric actuator that controls the extended cavity of the diode laser; parameters used are:

P(V/V)	I(V/V/ms)	D(V/(V·ms)
1.4	8	0

In both cases the technique used to optimize the parameters consists of

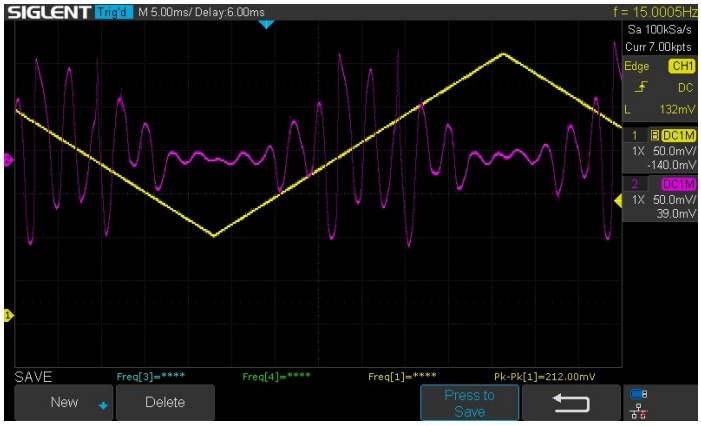

(a)

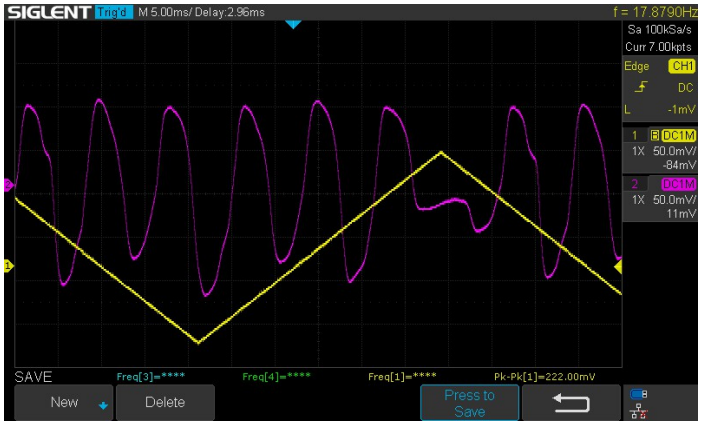

(b)

Figure 4.20. Error signals generated with 10 MHz low pass filter and 12 meters cable (a) and with 1.9 MHz low pass filter and 4 meters cable (b).

using as initial parameters the ones obtained via Ziegler-Nichols method and then optimize them manually. The lock stability was tested by perturbating the laser table and observing the response of the laser frequency. Finally, in perspective of performing the same procedure with the green laser, this does not pose a problem, since the main laser frequency can simply be shifted so that the beatnote signal matches the frequency obtained in the blue case.

Chapter 5

First observation of the atoms

The last chapter will focus on explaining the details relative to the alignment and the tuning of the Zeeman slower, the 2D MOTs and the imaging system that we had to implement to reach the first observation of atoms in the glass cell.

5.1 Atomic beam slowing and alignment

With the objective of transporting atoms into the glass cell, the most critical aspects are: the mechanical alignment of the AOsense atomic beam, the optical alignment of the Zeeman slower and the 2D MOTs, the beams polarization alignment, and the adjustment of the optical power of the Zeeman slower and of the 2D MOT. In the following, these issues are addressed individually, with a detailed discussion of the procedures performed in the laboratory.

The first thing to consider in order for lase slowing/cooling schemes discussed in chapter 1 is the light polarization. For the laser beams of both Zeeman slower and 2D MOTs the needed polarization is given by the manufacturer and it is right-handed circular. To set the polarization to circular we used the arrangement already presented in Fig. 4.2. For each beam we rotated the quarter-wave plate (QWP) until the retroreflected beam, after traversing the QWP a second time, had a linear polarization orthogonal to that of the incident beam at the polarizing beam splitter (PBS). The principle is the following: every QWP has two main axes, called fast and slow axes. A linearly polarized incident beam whose polarization has arbitrary angle α with respect to the wave-plate main axes is converted to elliptical polarization except for two cases: if α is 0° (polarization is aligned with one of the axes), then the wave-plate will have no effect, while if α is 45°, the output will be circularly polarized (right-handed if the angle is 45° with respect to the fast axis, left-handed if it is -45° with respect to the fast axis). This also means that, if α is 45° and the beam crosses the same waveplate again after backreflection from a mirror, the retroreflection after the second pass will be linearly polarized but orthogonal to the original one; hence, maximizing the reflection (if the input beam was transmitted) or the transmission (if the input beam was reflected) on the PBS

will make sure that the beam entering the window is circularly polarized. Now, all three beams are circularly polarized, but we don't know the direction of the polarization. To overcome this problem, we use the setup shown in Fig. 5.1.

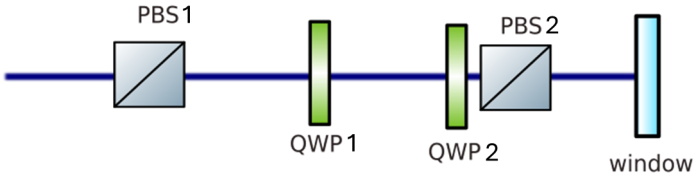

Figure 5.1. Simplified schematics of the setup used to tune the circular polarization.

The only difference is the presence of another pair of quarter-waveplate and polarizing beam splitter that in the figure are called QWP2 and PBS2. The procedure is the following: we place the new pair of QWP2 and PBS2 before the vacuum entrance window of one of the beams, that we will call beam 1, after having made sure it is circularly polarized using the method described above with QWP1 and PBS1. Then we rotate the QWP2 until the retroreflected beam is entirely reflected by PBS2. This means that the QWP2 angle is the same as the QWP1 angle, because it has the same effect of a double pass through PBS1 only. Now, we move the QWP2 and PBS2 pair to one of the other two beams in the same configuration and we call it beam 2. Its polarizing beam splitter and quarter-waveplate will be called PBS3 and QWP3 and they are placed in the same configuration as PBS1 and QWP1 for beam 1. If beam 2, after reflection on the window is transmitted through the PBS2, it means that the angle of the two quarter-waveplates (QWP2 and QWP3) is the opposite (45° and -45°) and, consequently, the polarization immediately after QWP3 is circular in the opposite direction of beam 1 polarization after QWP1. Now we rotate the QWP3 until the retroreflected beam is reflected by the PBS2, ensuring that the polarizations of beam 1 and 2 are the same. Finally, we do the same thing for the last beam. After all this procedure, we are sure that Zeeman slower and 2D MOTs have all the same circular polarization but we do not know if it is right-handed or left-handed, meaning we just have to try both ways.

Regarding the optical alignment, the Zeeman slower and the 2D MOTs are aligned checking the superposition of window-reflected beams with the incoming beams at long distances, to be sure they enter orthogonal to the waveplates. Once a first rough alignment is done we are able to observe by eye a fluorescence from the AOsense windows scanning the laser over the atomic transition. Since the beams are large, to fine-tune the alignment, we use irises to make the beams small (around 1 mm) and we checked again the superposition of incoming and reflected beam. Once this is done, using a camera focused right after the 2D MOTs, a clear beam can be seen in the AOsense chamber as shown in Fig. 5.2. The hole visible in figure, is the entrance to the tube that leads to the pumping chamber.

Finally, the last step was mechanical realignment of the AOsense chamber with respect to the glass cell, that was possible thanks to a camera place

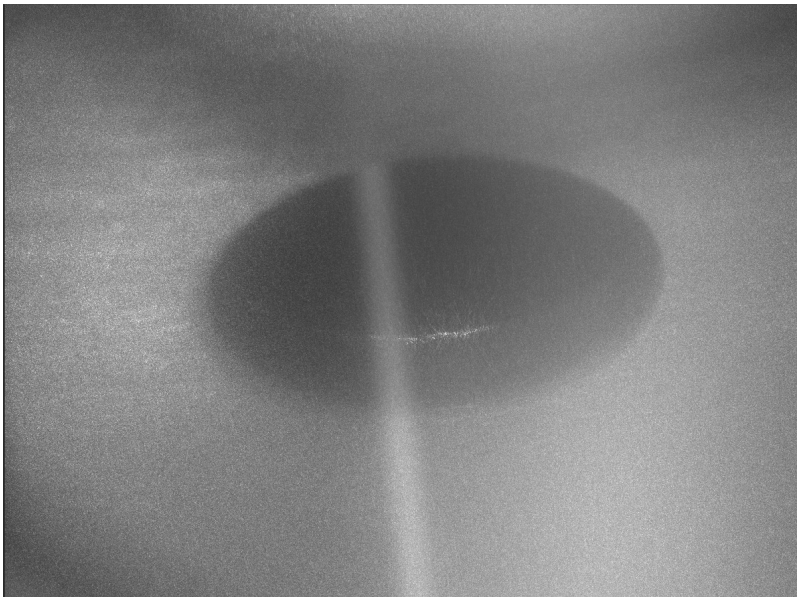

Figure 5.2. First observation of an atomic beam inside the AOsense. The beam is entering the tube that drives to the pumping chamber.

at the end of the glass cell and pointed towards the pumping chamber with focus at infinite distance. Here, by watching the reflections of the fluorescence on the tube between the pumping chamber and the AOsense chamber, the AOsense chamber can be realigned properly, making sure that the atoms can pass through and arrive in the glass cell.

5.2 First attempts to detect atoms in the glass cell

The next step is observing the atoms in the glass cell and fine-tune all the parameters presented in the last section in order to maximize the signal in the glass.

The first imaging setup implemented is constituted just by the imaging beam propagating along the cell and a Thorlabs camera pointed in the same direction through a polarizing beam splitter as shown in Fig. 5.3.

The polarizing beam splitter allows for the imaging beam to be aligned along the same path as the camera. The imaging power is the same as in the previous configuration, while the beam diameter varies. We try First a bigger beam diameter of around 3-4 mm, but since it is bigger than the diameter of the tube between pumping chamber and AOsense, some unwanted reflections cover the signal. With a smaller beam of around 1 mm, the beam passes through the tube. Since the beam is along the direction of propagation of the atomic beam, in order to be sure to resonantly excite the atoms, the imaging beam is scanned over a frequency span much bigger than the expected Doppler shift. In this case no signal is detected.

A second attempt is done in a new configuration, where the imaging beam

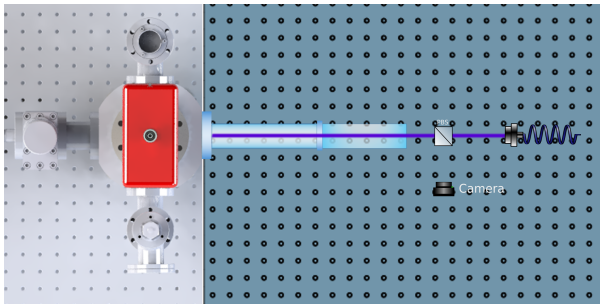

Figure 5.3. The first setup employed for imaging the beam in the glass cell. The camera is focused at infinity and pointed to the glass cell, meaning it detects fluorescence collected along the whole path inside the glass cell and the pumping chamber. The imaging beam is aligned towards the AOsense.

is vertical and the camera is focused at the intersection between the imaging beam and the center of the glass cell as shown in Fig. 5.4.

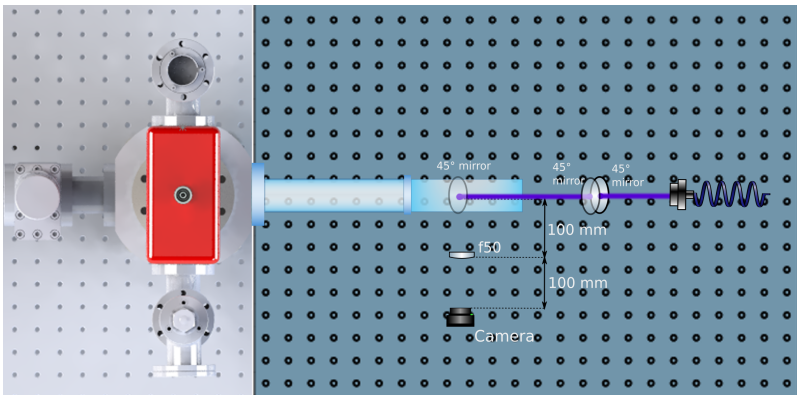

(a) View from above.

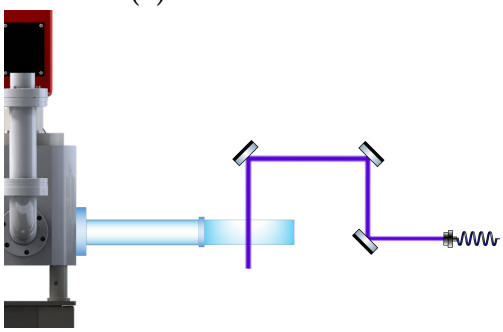

(b) View from the side.

Figure 5.4. The first setup employed for imaging the beam in the glass cell. The imaging beam arrives vertical in the cell, perpendicular to the atomic beam propagation direction, meaning the detuning from resonance has to be 0. the camera is placed on the side of the cell and focused on the position where the imaging beam crosses the center of the glass cell. Both views can be observed: (a) from above and (b) from the side.

The imaging beam power is few mW and its beam diameter at $1/e^2$ is ~ 2

mm. Since the beam is vertical and it is aligned as perpendicular as possible to the glass cell, no Doppler shift is considered, thus, the imaging beam detuning is set to zero from resonance 0. With this configuration, the first fluorescence signal has been observed. In particular, as shown in Fig. 5.5, by scanning the imaging beam detuning a clear atomic beam can be seen.

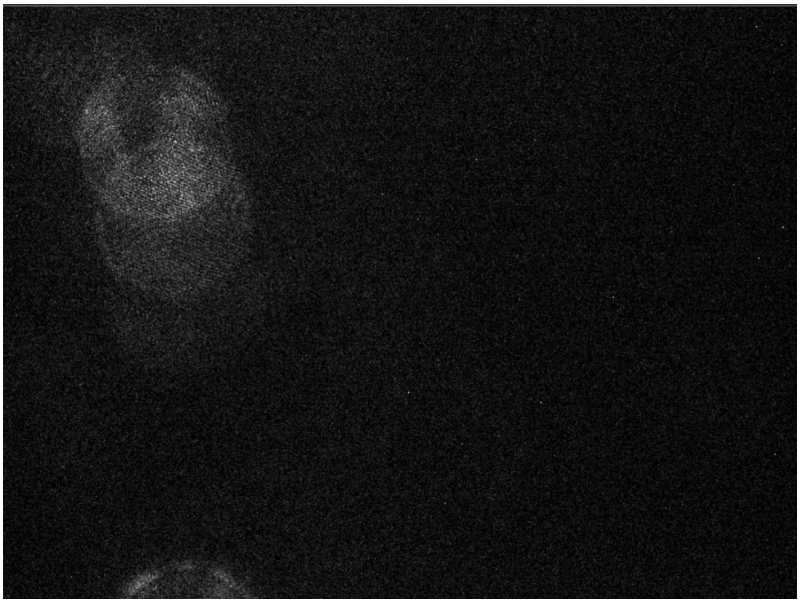

(a)

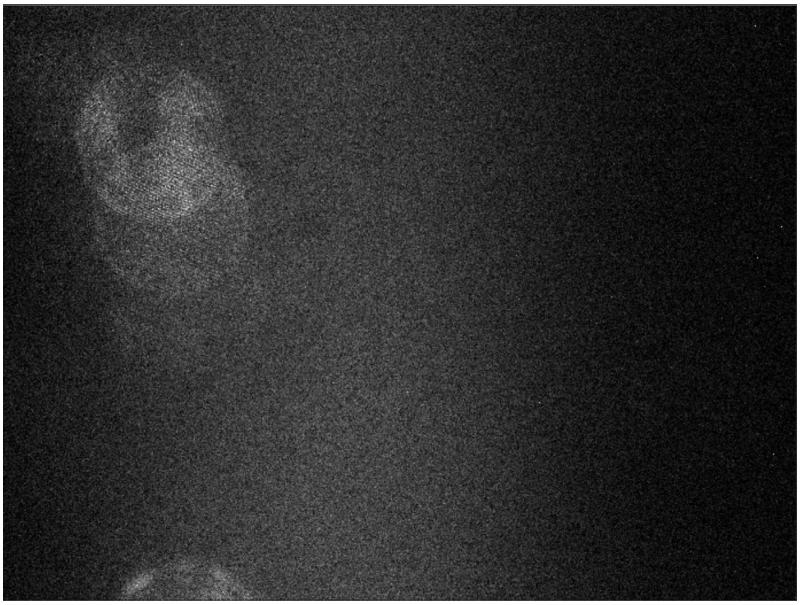

(b)

Figure 5.5. First fluorescence detection of atoms. The imaging beam detuning is scanned, leading to observation of a 'blinking' atomic beam signal. In (a) the signal is absent because the imaging beam is out of resonance, in (b) the imaging beam is resonant, leading to the observation of an atomic beam fluorescence.

Once the signal is observed, it is used to fine-tune all the parameters of the atomic beam alignment (beam polarizations, optical alignment, power) in order to optimized the signal in the cell.

5.3 399 nm 3D MOT

Since the signal found with the detection technique described in the previous sections is weak, before proceeding to the next trapping steps (green 556 nm 3D MOT), we decided to further optimize the signal building a 399 nm MOT (even if it will not be part of the final setup). The 399 nm 3D MOT collects the atoms in the cell increasing the atom density and, by consequence, the fluorescence signal. The MOT setup is shown in Fig. 5.6.

The 3D MOT is formed by three retro-reflected beams. Two of these beams lie in the same plane (parallel to the optical table); they are each inclined by 45° with respect to the glass cell axis and are orthogonal to one another. The third beam is directed perpendicular to that plane, providing the axial cooling axis. Retro-reflection of each beam produces the counter-propagating field pairs required for a standard six-beam MOT geometry. The magnetic quadrupole field is generated by a pair of coils in an anti-Helmholtz configuration, mounted above and below the glass cell; the coils are positioned so that their center coincides with the crossing point of the three beams to ensure a zero-field center at the atom cloud and optimal restoring forces.

The MOT beam $1/e^2$ waist is ~ 2.5 mm and the total optical power in the three beams is approximately 50 mW. The two beams that are parallel to the optical table are right-hand circularly polarized, as required for the chosen trapping transition, while the vertical one, since the magnetic field in the coils axis is the opposite (directed to the center instead of outwards), is left-handed circularly polarized. The beams are red-detuned by $\sim 1.3\ \Gamma$ (where Γ is linewidth of the transition), which is ~ -40 MHz. Two cameras are used for diagnostics (see Fig. 5.6a): a side-view camera is first employed to maximize the fluorescence signal from the trap, and once a sufficient signal level is achieved, a second camera, viewing the transmitted and then retroreflected vertical beam, is used to obtain absorption measurements.

An imaging beam that propagates through the glass cell is also overlapped with the MOT crossing position. It will be used in combination with the vertical beam to give an estimate of the atomic beam velocity in the glass cell, that will be necessary for the determination of the angle slowing beams characteristics that will guarantee that the atoms will slow down to the capture velocity of the 556 nm MOT (few m/s). This type of atomic beam velocity measurement works as follows. Briefly, it exploits the Doppler effect. When the probe (imaging) beam has a finite angle θ with respect to the atomic beam propagation direction, atoms moving at velocity v see the probe light Doppler-shifted by

$$\Delta\nu = \frac{v\cos\theta}{\lambda},$$

where λ is the probe wavelength. Thus atoms with velocity v are resonant

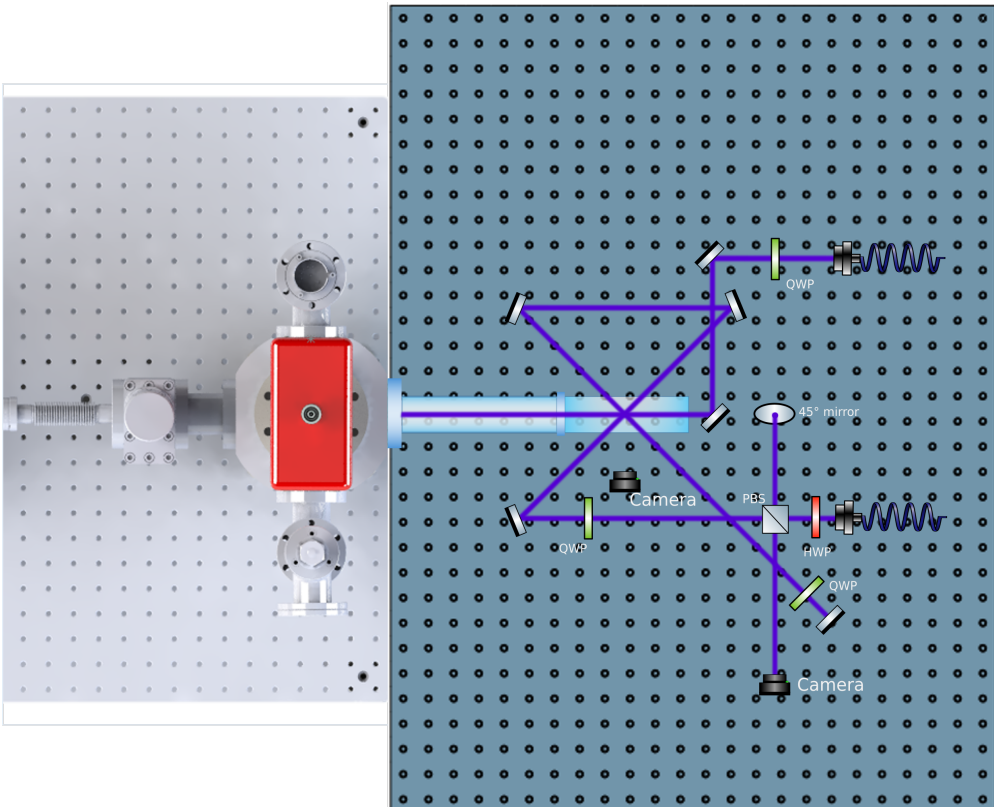

(a) MOT setup view from above.

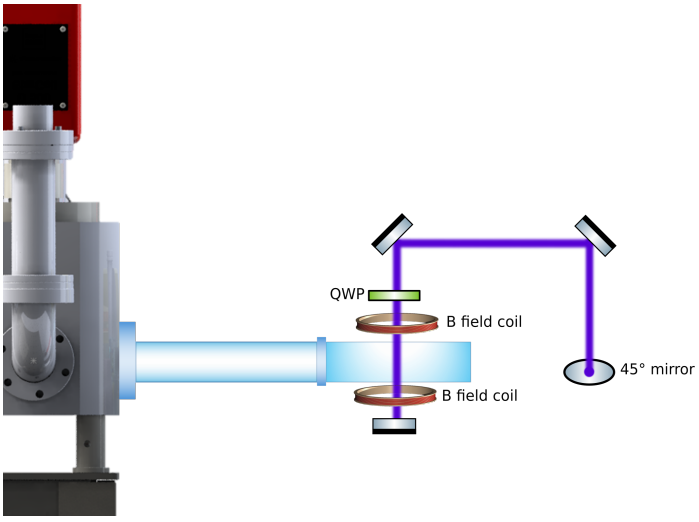

(b) MOT setup view from the side.

Figure 5.6. MOT setup. Three retroreflected beams create the 3D MOT. Two of them are parallel to the plane of the optical table, tilted by 45° with respect to the glass cell and by 90° with each other. The last beam is vertical, perpendicular to the others. Two coils positioned above and below the glass cell, create the magnetic field necessary for the MOT. Also the imaging beam is present, aligned along the direction of the cell.

with the probe when the probe detuning relative to the rest-frame resonance satisfies $\delta = \Delta\nu$. By scanning the probe detuning and recording the absorption (or fluorescence) signal, the experiment selects different velocity classes: the detuning that maximizes absorption at a given position corresponds to the mean velocity of atoms there.

In practice one proceeds as follows: the imaging beam is overlapped with the atomic beam, its frequency is scanned across resonance, and an absorption spectrum is recorded at the camera for each spatial region. A transverse resonance measurement (probe perpendicular to the atomic beam, $\theta = 90°$) gives the zero-shift reference frequency and the transverse linewidth (useful to quantify power broadening and transverse velocity spread). The longitudinal measurement (probe along the beam, $\theta \approx 0$) yields a resonance shifted by $\Delta\nu$. From the measured peak detuning δ_{peak} one obtains the mean propagation velocity

$$\bar{v} = \lambda\, \delta_{\text{peak}} / \cos\theta.$$

For higher accuracy the recorded line shapes should be fitted with an appropriate model (e.g. Voigt profile) to account for the convolution of the natural linewidth, power broadening and the velocity distribution; the fitted center gives the Doppler shift (hence $\bar{v}$) and the fitted width gives the longitudinal velocity spread.

From that estimate it is possible to derive the required parameters for the angled slowing beam needed to reach the 3D MOT capture velocity.

At the time of writing this thesis, the 3D 399 nm MOT has been built, but its being aligned and optimized. No clear trapped atoms signal has been obtained. The immediate next step will be the beam velocity measurement that was explained above, as it is fundamental for the finalization of the cooling and trapping apparatus.

Conclusions and next steps

This thesis reports the design, assembly and initial experimental activity carried out in a newly established atomic-physics laboratory aimed at developing a neutral-atom quantum-computing platform based on ^{171}Yb. The work presented here focused on the first stages of the experiment: the construction of the vacuum apparatus, the implementation of the laser systems required for the first cooling stages, the development of laser frequency stabilization schemes, and the preliminary attempts at atom trapping.

The vacuum apparatus was designed and assembled: a commercial Yb source is connected to a pumping chamber and a science cell. In the thesis the assembling process is thoroughly explained, starting from the basics component of ultra-high vacuum (pumps, ConFlat flanges) and then explaining the pumping process step by step: turbo pump rough pumping, bakeout, activation of ion pumps and getters. Furthermore, every component of the vacuum system is described with all its specifications and role in the experiment.

The 399 nm blue laser system is presented in its entirety, with detailed optical paths. Each role of the laser is discussed, with particular attention to the spectroscopy, the frequency lock of the laser on the spectroscopy signal and the Zeeman slower and the 2D MOTs, that constitute the first cooling stages of the atoms and also deflect the atomic beam into the glass cell, allowing for the following cooling stages to be implemented there.

The 556 nm green laser system design is presented, even though it has not been completed yet. The 1112 nm output at the seed laser frequency has been already used for the frequency locking of the laser and it is explained in detail, including the design of the optical paths built and the locking schemes. Particular attention is given to the reference cavity, which is an ultra-low expansion cavity, and to the implementation of Pound-Drever-Hall technique for the frequency lock on the cavity signal peaks. Furthermore, a second locking technique, the offset lock, is illustrated. As test of the technique, the 399 nm laser is frequency locked to a reference signal given by the beatnote between the laser to be stabilized and a reference laser (which is already locked on the frequency and with the stabilization needed).

Finally, the first observation of atoms in the glass cell is presented, explaining all the steps needed to reach it. Here, the alignment and tuning of the

relevant parameters for the cooling and deflection of the atoms into the glass cell are explained, from the beams polarization to the fine tuning of the beams optical alignment and the mechanical alignment of the AOsense chamber with the glass cell. The detection methods used to observe the atoms in the glass cell are also presented, including the first observation of atoms by fluorescence detection. Also the implementation of a 399 nm 3D MOT with the purpose of optimizing the atoms density in the glass described, with the propose of the beam velocity measurement, that will be the immediate next step after optimization.

After these first stages of the experiment implemented during this thesis the roadmap for the next steps is:

1. After performing the beam velocity measurement proposed in chapter 5, angle slowing will be implemented and tuned in a way to guarantee that the atoms reach the few m/s capture velocity of the 556 nm green MOT.

2. Building of the green laser system and implementation of the 3D green MOT on the 556 nm Ytterbium transition. It will lay the groundwork for the subsequent development of the optical tweezers system.

3. Testing of the high numerical aperture objectives and first implementation of optical tweezers. In this step also various algorithms for the loading and rearrangement of the atoms trapped in optical tweezers will be tested, trying to reach the loading rates demonstrated in state of the art experiments with the so called near deterministic loading schemes [28].

4. Finally, we will start working on qubits and gates. Qubit initialization and single-qubit gates will be implemented, exploring different Raman transition schemes for both the ground and the clock state qubits. Furthermore, several possibilities for the implementation of selective excitations will be explored.

5. Multi-qubit gates implementation. Starting from two-qubit interaction, Rydberg excitations physics will be explored, trying to create the most stable and fast gates possible.

In conclusion, this newly established laboratory will offer excellent opportunities to explore new physics in a rapidly growing field that is attracting great attention due to its vast potential to address problems of both fundamental and industrial interest that are currently beyond the reach of classical technologies.

Bibliography

[1] M. Morgado and S. Whitlock. "Quantum simulation and computing with Rydberg-interacting qubits". In: *AVS Quantum Science* 3.2 (May 2021). ISSN: 2639-0213. DOI: 10.1116/5.0036562. URL: http://dx.doi.org/10.1116/5.0036562.

[2] F. Nogrette et al. "Single-Atom Trapping in Holographic 2D Arrays of Microtraps with Arbitrary Geometries". In: *Phys. Rev. X* 4 (2 May 2014), p. 021034. DOI: 10.1103/PhysRevX.4.021034. URL: https://link.aps.org/doi/10.1103/PhysRevX.4.021034.

[3] Sepehr Ebadi et al. "Quantum phases of matter on a 256-atom programmable quantum simulator". In: *Nature* 595.7866 (July 2021), pp. 227–232. ISSN: 1476-4687. DOI: 10.1038/s41586-021-03582-4. URL: http://dx.doi.org/10.1038/s41586-021-03582-4.

[4] Hannah J. Manetsch et al. *A tweezer array with 6100 highly coherent atomic qubits*. 2024. arXiv: 2403.12021 [quant-ph]. URL: https://arxiv.org/abs/2403.12021.

[5] D.A. Steck. *Quantum and Atom Optics*. 2007. URL: https://books.google.it/books?id=bc9TMwEACAAJ.

[6] Adam Kaufman and Kang-Kuen Ni. "Quantum science with optical tweezer arrays of ultracold atoms and molecules". In: *Nature Physics* 17 (Nov. 2021). DOI: 10.1038/s41567-021-01357-2.

[7] Manuel Endres et al. "Atom-by-atom assembly of defect-free one-dimensional cold atom arrays". In: *Science* 354 (2016), pp. 1024–1027. URL: https://api.semanticscholar.org/CorpusID:4035684.

[8] Kevin M. Jones et al. "Ultracold photoassociation spectroscopy: Long-range molecules and atomic scattering". In: *Rev. Mod. Phys.* 78 (2 May 2006), pp. 483–535. DOI: 10.1103/RevModPhys.78.483. URL: https://link.aps.org/doi/10.1103/RevModPhys.78.483.

[9] A. Fuhrmanek et al. "Light-assisted collisions between a few cold atoms in a microscopic dipole trap". In: *Phys. Rev. A* 85 (6 June 2012), p. 062708. DOI: 10.1103/PhysRevA.85.062708. URL: https://link.aps.org/doi/10.1103/PhysRevA.85.062708.

[10] F. Nogrette et al. “Single-Atom Trapping in Holographic 2D Arrays of Microtraps with Arbitrary Geometries”. In: *Phys. Rev. X* 4 (2 May 2014), p. 021034. DOI: 10.1103/PhysRevX.4.021034. URL: https://link.aps.org/doi/10.1103/PhysRevX.4.021034.

[11] Daniel Barredo et al. “An atom-by-atom assembler of defect-free arbitrary two-dimensional atomic arrays”. In: *Science* 354.6315 (Nov. 2016), pp. 1021–1023. ISSN: 1095-9203. DOI: 10.1126/science.aah3778. URL: http://dx.doi.org/10.1126/science.aah3778.

[12] John Bechhoefer. “Feedback for physicists: A tutorial essay on control”. In: *Rev. Mod. Phys.* 77 (3 Aug. 2005), pp. 783–836. DOI: 10.1103/RevModPhys.77.783. URL: https://link.aps.org/doi/10.1103/RevModPhys.77.783.

[13] By J. G. Ziegler and Nathaniel B. Nichols. “Optimum Settings for Automatic Controllers”. In: *Journal of Fluids Engineering* (1942). URL: https://api.semanticscholar.org/CorpusID:41336178.

[14] R.W.P. Drever et al. “Laser Phase and Frequency Stabilization Using an Optical Resonator”. In: *Appl. Phys. B* 31 (June 1983), pp. 97–105. DOI: 10.1007/BF00702605.

[15] Eric Black. “An introduction to Pound-Drever-Hall laser frequency stabilization”. In: *American Journal of Physics* 69 (Jan. 2001), pp. 79–87. DOI: 10.1119/1.1286663.

[16] Thomas F. Gallagher. “Rydberg atom wavefunctions”. In: *Rydberg Atoms*. Cambridge Monographs on Atomic, Molecular and Chemical Physics. Cambridge University Press, 1994, pp. 10–26.

[17] Jack Wilson. “New tools for quantum science in Yb Rydberg atom arrays”. PhD thesis. Princeton University, 2022.

[18] D. Jaksch et al. “Fast Quantum Gates for Neutral Atoms”. In: *Phys. Rev. Lett.* 85 (10 Sept. 2000), pp. 2208–2211. DOI: 10.1103/PhysRevLett.85.2208. URL: https://link.aps.org/doi/10.1103/PhysRevLett.85.2208.

[19] Michael A. Nielsen and Isaac L. Chuang. *Quantum Computation and Quantum Information: 10th Anniversary Edition*. Cambridge University Press, 2010.

[20] Alec Jenkins et al. “Ytterbium Nuclear-Spin Qubits in an Optical Tweezer Array”. In: *Physical Review X* 12.2 (May 2022). ISSN: 2160-3308. DOI: 10.1103/physrevx.12.021027. URL: http://dx.doi.org/10.1103/PhysRevX.12.021027.

[21] M. Saffman, T. G. Walker, and K. Mølmer. “Quantum information with Rydberg atoms”. In: *Rev. Mod. Phys.* 82 (3 Aug. 2010), pp. 2313–2363. DOI: 10.1103/RevModPhys.82.2313. URL: https://link.aps.org/doi/10.1103/RevModPhys.82.2313.

[22] Harry Levine et al. "Parallel Implementation of High-Fidelity Multiqubit Gates with Neutral Atoms". In: *Physical Review Letters* 123 (Oct. 2019). DOI: 10.1103/PhysRevLett.123.170503.

[23] Sven Jandura and Guido Pupillo. "Time-Optimal Two- and Three-Qubit Gates for Rydberg Atoms". In: *Quantum* 6 (May 2022), p. 712. ISSN: 2521-327X. DOI: 10.22331/q-2022-05-13-712. URL: http://dx.doi.org/10.22331/q-2022-05-13-712.

[24] Adam L. Shaw et al. "Dark-State Enhanced Loading of an Optical Tweezer Array". In: *Phys. Rev. Lett.* 130 (19 May 2023), p. 193402. DOI: 10.1103/PhysRevLett.130.193402. URL: https://link.aps.org/doi/10.1103/PhysRevLett.130.193402.

[25] Joanna W. Lis et al. "Midcircuit Operations Using the omg Architecture in Neutral Atom Arrays". In: *Phys. Rev. X* 13 (4 Nov. 2023), p. 041035. DOI: 10.1103/PhysRevX.13.041035. URL: https://link.aps.org/doi/10.1103/PhysRevX.13.041035.

[26] Adam Lawrence Shaw. "Learning, Verifying, and Erasing Errors on a Chaotic and Highly Entangled Programmable Quantum Simulator". PhD thesis. Caltech, 2024. DOI: 10.7907/t7jr-mf97.

[27] U. Schunemann et al. "Simple scheme for tunable frequency offset locking of two lasers". In: *Review of Scientific Instruments* 70 (Feb. 1999), pp. 242–243. DOI: 10.1063/1.1149573.

[28] Xu Yan et al. "Multi-reservoir enhanced loading of tweezer atom arrays". In: *Phys. Rev. Res.* 7 (1 Jan. 2025), p. 013031. DOI: 10.1103/PhysRevResearch.7.013031. URL: https://link.aps.org/doi/10.1103/PhysRevResearch.7.013031.

Ringraziamenti

In questa pagina finale della tesi vorrei ringraziare tutte le persone che hanno partecipato a questo percorso e, direttamente o indirettamente, hanno contribuito all'arrivo a questo punto.

Innanzitutto ringrazio Leonardo, Luca, Wies, Andy e gli altri del gruppo perché quando ne ho avuto bisogno, sia durante tutta la tesi, che per la preparazione del progetto di dottorato, sono sempre stati disponibili ad aiutarmi. In particolare un grazie a Krish e Thomas, che hanno sempre trovato tempo di spiegarmi e insegnarmi tutto ciò di cui avevo bisogno per l'esperimento e per i miei primi giorni da fisico sperimentale in un laboratorio dove a ogni passo rischiavo di spaccare qualcosa.

Un grande grazie va anche alla mia famiglia, che mi ha permesso di vivere la mia vita universitaria senza preoccuparmi di nulla e dandomi sempre sostegno per qualsiasi cosa (soprattutto per la grana), rispettando, pure senza quasi mai lamentarsi, i miei bisogni di spazio e silenzio tombale in casa in occasione della preparazione degli esami.

Grazie a Duccio, Ele e Gabri con cui, anche se non partecipando direttamente alla mia vita universitaria, ho condiviso alcuni dei momenti più importanti di questi anni.

Grazie a tutti gli amici dell'università, pipscarraldo, Giova, Ame e tutti gli altri con cui ho condiviso il percorso finora più importante e impegnativo della mia vita. Grazie per avermi permesso di divertirmi più di quanto pensassi fosse possibile in mezzo a esami e sessioni intensive di studio (e soprattutto di calcino).

Infine l'ultimo e più grande grazie a Marta che, anche se un po' scorbutica, è sempre stata presente e mi ha sostenuto per qualsiasi cosa volessi o dovessi fare, sacrificando il suo tempo per aiutarmi ogni volta che avevo bisogno, per calmarmi quando avevo ansia per esami, per entusiarmarsi per ogni disegno e animazione per cui perdevo ore nelle presentazioni, per servirmi e riverirmi quando non avevo neanche il tempo di respirare. Grazie per aver condiviso con me i momenti peggiori e migliori di questi anni, strappandomi un sorriso anche nei periodi più difficili. Posso affermare con relativa certezza che senza di te sarei probabilmente ancora a metà percorso a chiedermi se sia possibile arrivare in fondo.